Computational Investigation of Abstraction in Claude Monet's *Water Lilies* through Brushstroke Analysis

Jia Li, *Fellow, IEEE,* Chaewan Chun, Kathryn Brown, and James Z. Wang, *Senior Member, IEEE*

Abstract—Claude Monet's late paintings of *Water Lilies* exhibit stylistic transformations that are often characterized by art historians as increasingly abstract and gesturally expressive. However, it remains challenging to define and systematically identify this stylistic shift. Here, we introduce a machine learning framework for analyzing Monet's evolving brushwork using streamline curves: computational representations that capture the dynamic movement patterns inherent in brushstrokes. From 554 image patches sampled from 47 paintings spanning early (pre-1913) and later (post-1913) periods of Monet's output, we extract streamlines and compute geometric features for each, including smoothness of curvature and directional variability. Each image is represented as a set of streamline feature vectors, a data type referred to as distributional. A new deep neural network architecture named Composition to Attribute (C2A) is designed for classifying distributional data. We hypothesize that Monet's so-called 'abstract' style does not uniformly characterize all late-period *Water Lilies*, and that non-abstract flowers, regardless of period, share similar brushwork qualities. Under these assumptions, building on C2A, we propose a novel learning paradigm named Discover Embedded Group with Asymmetry (DEGA) which enforces a shared distribution of DNN-extracted features for non-abstract flower patches across both periods while distinguishing the abstract ones. DEGA reveals a meaningful two-dimensional feature space, where one dimension differentiates abstract from mimetic *Water Lilies*, while the other separates abstract flowers from close-up flowers of the early period. Our findings suggest that the so-called 'abstract' qualities of Monet's late style retain certain visual affinities with his earlier approach to depicting close-up floral motifs. When this brushwork is used in more expansive scenes, the depiction of flowers shifts away from realistic renderings of individual petals toward a looser, more allusive expression, conveying a sense of floral presence rather than botanical detail. This study highlights the value of computational analysis for a more accurate understanding of an artist's stylistic development.

Index Terms—Computational art analysis, style analysis, brushstroke modeling, abstractness, oil paintings, streamline.

1 INTRODUCTION

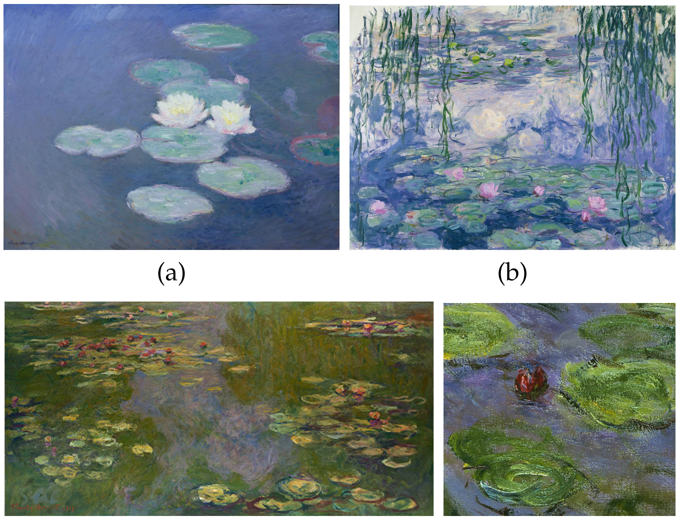
(a) (b)
(c) (d)

Fig. 1. Selections from Claude Monet's *Water Lilies* (French: *Nymphéas*). (a) *Water Lilies—Evening Effect*, 1897, oil on canvas, 73 × 100 cm, Musée Marmottan Monet. (b) c. 1916–1919, oil on canvas, 150 × 197 cm, Musée Marmottan Monet. (c) 1919, oil on canvas, 101 × 200 cm, Metropolitan Museum of Art. (d) Detail showing intermingled brushstrokes, c. 1914–1917, oil on canvas, National Gallery of Australia.

FROM the 1890s until his death, French Impressionist Claude Monet (1840–1926) created paintings with increasingly textured and abstract surfaces (Fig. 1). In 1912, he developed cataracts that significantly affected his sight. In 1914, at age 74, he radically reinvented his style and, by 1922, described working in a "complete fog" [1]. These physiological changes and stylistic shifts, coupled with Monet's tendency to rework paintings, make many of his late *Water Lilies* canvases difficult to date.

A fundamental question in art history concerns the *evolution* of Monet's brushstroke techniques and *compositional*

J. Li is with the Department of Statistics and (by courtesy) Computer Science and Engineering, The Pennsylvania State University, University Park, PA, 16803 USA e-mail: jiali@stat.psu.edu.
C. Chun and J. Z. Wang are with the College of Information Sciences and Technology, The Pennsylvania State University, University Park, PA, 16803 USA e-mails: czc5884@psu.edu, jwang@ist.psu.edu.
K. Brown is with the School of Social Sciences and Humanities, Loughborough University, the United Kingdom. e-mail: K.J.Brown@lboro.ac.uk
The A.I. and computer vision research of J. Li, C. Chun, and J. Z. Wang has been supported by the National Science Foundation (NSF) under Award No. 2234195. The explainable A.I. research of J. Li has been supported by the NSF under Award No. 2205004. This work used cluster computers at the National Center for Supercomputing Applications and the Pittsburgh Supercomputing Center through an allocation from the Advanced Cyberinfrastructure Coordination Ecosystem: Services & Support (ACCESS) program, which is supported by NSF Award Nos. 2138259, 2138286, 2138307, 2137603, and 2138296. Kathryn Brown thanks the British Academy for supporting the initial stages of this research (Award No. TDA21:210060). The authors are grateful to the reviewers and the associate editor for their thoughtful and constructive comments.
Manuscript received June 1, 2025; revised December 1, 2025, accepted February 9, 2026.

practices in his *Water Lilies*, produced from the 1890s to 1926. These works were inspired by the private garden that the artist created at his home in Giverny, where he had settled in 1883. Over the ensuing decades, Monet treated the subject of the water lilies and their environment in around 250 paintings, over 40 of which are large-format compositions. The *Water Lilies* were chosen for this study not only because they showcase some of Monet's most adventurous and expressive brushwork, but also because the water lily itself is a distinct and recurring motif on which to focus over three decades of the artist's career. This allows for the extraction of visual information across canvases to isolate Monet's different renderings of, and pictorial approaches to, this motif.

Numerous approaches have been developed by researchers in computer vision and machine intelligence for the computational analysis of paintings. Without intending to exhaust the list, we refer readers to [2], [3] for high-level overviews and highlight some notable examples [4], [5], [6], [7], [8]. Despite the wealth of research in this field, a persistent challenge remains: the analysis of brushstrokes that are intermingled and difficult to distinguish. For instance, in the study by Li et al. [9], brushstrokes were successfully extracted from Vincent van Gogh's paintings; however, the authors were unable to extract strokes from many regions of the canvases and observed a significantly lower extraction rate from the works of Van Gogh's contemporaries, largely due to the lower visual separability of their strokes. In a recent study on John Constable's *Cloud Studies*, Zhang et al. [10] circumvented brushstroke-level analysis altogether.

To tackle our art-historical question, i.e., to understand the stylistic evolution of Monet's *Water Lilies*, however, it is essential to examine the characteristics of the artist's brushstrokes, which serve as fundamental markers of his compositional technique and gestural approach to a key motif. Across the three decades over which these works were produced, Monet's handling of paint—its texture, directionality, density, and rhythm—underwent significant transformation. These changes are not always apparent at the level of composition or color alone, especially given the thematic and formal continuity of the series. Instead, they are often encoded in the *structure* of the brushwork, particularly in how paint traces move across the canvas (Fig. 1(d)). To capture these stylistic shifts, we need to develop a new method that is capable of detecting and analyzing the *dynamic qualities* of brushstrokes. This motivated our development of a computational approach based on streamline detection, which models brushstroke flow as coherent directional patterns.

Analyzing Monet's stylistic evolution requires an explainable framework that not only captures visual patterns but also makes them intelligible to art scholars. In particular, analyzing the streamlines of brushstrokes (continuous directional flows that structure the surface of the Water Lilies) demands a method sensitive to painterly gesture and transparent in its reasoning. By developing a new explainable approach, we aim to bridge the gap between computational analysis and humanistic interpretation, enabling a more meaningful dialogue between algorithmic output and art-historical insight.

1.1 Related Work

Earlier work on computer-based analysis of paintings has been reviewed in a survey [3]. In this paper, we focus on more recent developments, particularly those leveraging deep neural networks (DNNs) to characterize artistic style.

A survey [11] discusses a wide range of DNN applications for visual art analysis and generation. Many of these works address classification of content, authorship, and style. Regarding artistic style, two major areas of research have emerged: style classification [12], [13] and style transfer [14], [15], [16]. Most existing approaches assume that style is expressed through global visual patterns—such as color schemes, textures, or brushstroke orientations across entire paintings—rather than through nuanced variations in how specific objects are depicted. For example, stylistic distinctions may be defined by slanted versus swirling brushstrokes, or by contrasting color palettes (e.g., warm versus cool tones). While these global features are effective for tasks like style transfer, they often fail to capture finer stylistic variations, especially those evident in the rendering of individual subjects (e.g., flowers) within a composition.

Another largely unexplored aspect of machine learning-based style analysis is the emergence of new artistic styles that art historians recognize but cannot clearly define or assign to specific periods in an artist's output. From a learning perspective, this poses a challenge because no labeled data indicate which images (or image regions) belong to an artist's emergent style. Instead, discovery must rely on partial cues, such as temporal context. Our study is designed to address this challenge. In contrast to standard unsupervised clustering approaches (e.g. [17]), our work is situated within a specific art-historical context, and our objective differs: rather than clustering for its own sake, we aim to deepen historical interpretation of these complex canvases by developing a new approach to the identification and classification of stylistic changes and continuities.

Furthermore, we emphasize the importance of developing computational methods that help art historians characterize such styles through visual traits, specifically, detailed brushstroke qualities. Given the opacity of powerful yet hard-to-interpret DNNs, this poses a particularly demanding problem. Most existing DNN-based approaches treat style classification as a black-box task, offering little insight into the visual features that drive their decisions.

Another important but underexplored aspect in this domain is the modeling of distributional data. In many settings, including art and medical informatics, the data of interest comprise distributions over local features (e.g., shapes, textures, or localized descriptors). Conventional approaches typically reduce these distributions to fixed-length vectors by computing summary statistics, such as cluster proportions or mean embeddings, before applying standard classifiers. Recent studies in medical informatics [18], [19] have sought to preserve more structure by treating distributions as two-dimensional arrays, analogous to images, and applying convolutional neural networks (CNNs). However, these representations often rely on arbitrary subsampling and row ordering, introducing artifacts and assumptions that are not semantically meaningful. As a result, such models remain opaque and potentially misleading.

In contrast, our proposed network architecture is explicitly designed to respect the distributional nature of the input data. It is invariant to permutations of the input rows and hence avoids imposing an artificial structure. This design choice significantly enhances the explainability of the model. Our framework is flexible: it can be used as a black-box predictor optimized for classification accuracy or as an interpretable model capable of revealing which features drive the decisions. This interpretability is particularly important in our context, where the goal is not simply to classify style but to understand the nature of stylistic development and its implications for conceptions of a particular artist's creative output.

Critical evaluations of Monet's *Water Lilies* typically describe the artist's style as developing from naturalism to abstraction. As early as 1909, the art critic Pierre Mille discussed the distinctive 'physiognomies' of Monet's water lilies and the visual metamorphoses they underwent in Monet's 'magical' waterscapes [20]. In 1923, Louis Vauxcelles suggested that light "devoured the contours" of objects in Monet's paintings [21]. By 1927, Louis Gillet argued that Monet's paintings of his water lily pond could not have been executed "after nature" and that, in consequence, "pure abstraction could go no further" [22]. Five years later, the critic and curator Paul Jamot argued that Monet's art demonstrated a pictorial evolution from realism to "surrealism" in which the artist was clearly no longer interested in the object of depiction [23]. Running throughout these critical responses is the idea that Monet gradually practised a *process* of abstraction by incrementally removing information from his depictions of the visible world. To critics who had grown up in the art world of the mid- to late nineteenth century, this marked Monet as a radically inventive artist.

The premise that the latter decades of Monet's career were characterized by an abstract style has also been debated by more recent art critics, historians, and museum curators. Exhibitions in Europe and the US have made connections between Monet's late works and abstract paintings by twentieth-century artists including Cy Twombly [24], Jackson Pollock [25], and Joan Mitchell [26]. This trend reinforces an interpretation of Monet that the American critic Clement Greenberg proposed in the 1950s in his discussion of the late *Water Lilies*: "What he [Monet] found in the end was [. . .] not so much a new as a more comprehensive principle; and it lay not in Nature, as he thought, but in the essence of art itself, in art's 'abstractness'. That he himself could not recognize this makes no difference" [27]. In Greenberg's account, Monet gradually became an abstract painter in spite of himself.

In this work, we investigate the contribution that computational methods can add to these qualitative accounts of the development of Monet's style and his painterly approach to rendering information about the visible world. We use a conception of 'abstract' as the reduction of pictorial information about a real-world object (a water lily) in brushmarks that retain an isomorphic relation to that object.

1.2 Our Contributions

The main **technical contributions** of our work are as follows.

- *A novel algorithm for extracting streamline curves in painted brushwork.* We introduce a computational method to detect and characterize streamline curves—coherent directional patterns—in painted brushstrokes. Our approach robustly captures brushstroke dynamics for a wide range of oil paintings, enabling quantitative style analysis previously unattainable at the brushstroke level.
- *A DNN architecture tailored for classifying distributional data.* We propose the Composition to Attribute (C2A) neural network, specifically designed to classify complex distributional data representing brushstroke dynamics. Unlike conventional neural networks, C2A effectively learns from sets of geometric feature vectors extracted from streamline curves.
- *A framework for identifying subgroups with asymmetric relationships to labeled classes.* We introduce Discover Embedded Group with Asymmetry (DEGA), a novel learning paradigm that isolates stylistic subgroups exhibiting asymmetric relationships with predefined classes. DEGA enforces shared feature distributions across related classes, clearly distinguishing subgroups such as abstract from non-abstract paintings.

These techniques form a new explainable framework for studying stylistic evolution through brushstroke dynamics. Unlike existing methods that rely on opaque feature representations or classification-driven models, our method emphasizes interpretability, enabling direct engagement with the gestural qualities of brushwork.

Our study offers fresh **art-historical insights** into Monet's stylistic evolution and compositional practices in the *Water Lilies*.

- *Holistic approach to style*: The discovery of brushstroke similarities across the rendering of early and late *Water Lilies* encourages a more holistic view of Monet's style. Rather than trying to force Monet's creative practice into distinct periods understood as 'Realist' or 'Abstract', our study demonstrates the existence of continuity in mark-making from early to late *Water Lilies*. This counters long received art-historical narratives that seek to identify a linear development towards an overall abstract style in Monet's output.
- *Importance of the water lily motif*: Demonstrating gestural continuities in the brushwork of the *Water Lilies* suggests that this motif serves as an important visual anchor that often offsets less naturalistic depictions of the relevant waterscape in which they are embedded. Rather than understanding entire paintings as either realistic or abstract renderings of the water lily pond and its flora, our study offers a more nuanced account of the variable styles of mark-making found within individual paintings. This avoids the imposition of unitary stylistic categories on Monet's works.
- *A new conception of Monet's pictorial logic*: Mapping streamlines in Monet's depictions of water lilies gives a clearer sense of the pictorial logic of the paintings that is not visible to the human eye. While some early critics of Monet's works thought that the paintings lacked a coherent, directional structure (i.e., that they could be turned upside down) [22], our analysis

gives a better sense of the flow of brushmarks and, hence, of the way in which the paintings were conceived and structured. This part of the analysis also has the potential to complement and extend conservation approaches to understanding the internal structure of the works.

The remainder of the paper is organized as follows. Section 2 describes the dataset and preprocessing steps, including how individual *Water Lilies* were identified and represented as distributions. Our network architecture and training method are presented in Section 3. Section 4 details the experimental setup and results, highlighting insights gained from interpreting the learning outcomes. In Section 5, we reflect on the implications of our findings for understanding stylistic evolution in Monet's art and their relevance to art-historical inquiry. Section 6 concludes and outlines promising directions for future research.

2 PRELIMINARIES

In our study, we examined a total of 47 Monet's *Water Lilies* belonging to two time periods: early (pre-1913) and late (post-1913). A catalog of these paintings, including their IDs used in our study, titles, physical dimensions, and current holding institutions, is provided in Supplementary Materials. We refer to the paintings by their IDs throughout the discussion. From these paintings, flower images were first manually cropped, but very small flowers were not used in our experiments, resulting in a collection of 554 flower images at the end. In the discussion below, we refer to a cropped flower image as a "patch." To avoid confusion, an entire painting will always be referred to as a "painting," not as an "image." The flowers in patches were then manually segmented by placing points around the flower boundaries. Automatic segmentation tools, such as Segment Anything [28], were not used because of their limited accuracy when object boundaries are complex and non-mimetic, as is common for Monet's depictions of water lilies.

An oil painter's style, technique, and expressive qualities emerge from their brushwork. Understanding brushstrokes is essential for distinguishing individual styles and tracing their evolution. One might question why we do not consider color; the reason is that color can be unreliable due to variations introduced during the digital reproduction of artworks. Additionally, color can fade over time, further complicating accurate analysis. An earlier study of Van Gogh's brushstrokes similarly excluded color from analysis to mitigate potential biases [9], [29].

Extracting complete brushstrokes from Monet's paintings is a daunting task—even for the human eye—owing to their fluid boundaries and complex layering. Instead, we focus on a finer-level characteristic: the bristle marks within brushstrokes, which more directly reflect the physical movement of the brush. These marks often span entire painted flowers, encoding subtle variations in direction and texture that offer insight into the artist's technique. To analyze their structure, we avoid the uncertain process of grouping marks into full strokes and instead model their directional flow directly. We developed a streamline-based method to capture this motion: the image is treated as a vector field from which the structure tensors are computed to encode dominant orientations of local intensity variation [30]. Streamlines—analogous to the paths that leaves might follow in a flowing stream—are then traced through this field. In this context, each streamline approximates the trajectory of a bristle mark, allowing us to reconstruct coherent, gesture-like paths across the surface of the painting. This computational approach provides a principled way to visualize and quantify stylistic attributes that are typically described qualitatively in art-historical analysis, offering new insight into the visual effects created by Monet's works.

Consider an image $I(\zeta,\eta)$, $\zeta = 1,...,n_w$, $\eta = 1,...,n_h$, where ζ and η denote the horizontal and vertical coordinates, respectively, and n_w and n_h represent the width and height of the image. Let I_ζ and I_η denote the two gradients, i.e., the partial derivatives of the intensity with respect to the two coordinates:

$$I_\zeta = \frac{\partial I(\zeta,\eta)}{\partial \zeta}, \quad I_\eta = \frac{\partial I(\zeta,\eta)}{\partial \eta} \ .$$

The structure tensor $J(\zeta,\eta)$, which summarizes the local gradient information at the coordinate (ζ,η), is defined as:

$$J(\zeta,\eta) = \begin{bmatrix} I_{\zeta\zeta} & I_{\zeta\eta} \\ I_{\zeta\eta} & I_{\eta\eta} \end{bmatrix} = \begin{bmatrix} \left(\frac{\partial I}{\partial \zeta}\right)^2 & \left(\frac{\partial I}{\partial \zeta}\frac{\partial I}{\partial \eta}\right) \\ \left(\frac{\partial I}{\partial \zeta}\frac{\partial I}{\partial \eta}\right) & \left(\frac{\partial I}{\partial \eta}\right)^2 \end{bmatrix} \ .$$

To obtain a robust estimation of local features and reduce sensitivity to noise, the structure tensor J is smoothed by Gaussian filtering with a standard deviation of 8.

The two eigenvectors of $J(\zeta,\eta)$ are computed to characterize local image structure. The first eigenvector, $\mathbf{u}_1(\zeta,\eta)$, associated with the larger eigenvalue $\lambda_1(\zeta,\eta)$, points in the direction of the greatest intensity variation at position (ζ,η) of $I(\zeta,\eta)$. The second eigenvector, $\mathbf{u}_2(\zeta,\eta)$, which is orthogonal to the first and corresponds to the smaller eigenvalue $\lambda_2(\zeta,\eta)$, indicates the direction of minimal change in $I(\zeta,\eta)$, and thus aligns with the local flow direction of the streamline. $\lambda_1(\zeta,\eta) \geq \lambda_2(\zeta,\eta)$. Note that $-\mathbf{u}_i(\zeta,\eta)$ is also a valid eigenvector associated with $\lambda_i(\zeta,\eta)$, due to the inherent sign ambiguity of eigenvectors.

We define the *eigen-ratio* as follows:

$$\kappa(\zeta,\eta) = \frac{\lambda_2(\zeta,\eta)}{\lambda_1(\zeta,\eta)} \ . \tag{1}$$

This ratio quantifies how strongly the image intensity $I(\zeta,\eta)$ varies along the direction of $\mathbf{u}_2(\zeta,\eta)$ relative to $\mathbf{u}_1(\zeta,\eta)$. A smaller eigen-ratio indicates a more pronounced anisotropy in the local variation, and hence a clearer flow direction.

Following the notation convention, we use $(\cdot,\cdot)$ to denote a row vector while $(\cdot,\cdot)^t$ to denote a column vector. In our discussion, $\mathbf{u}_i(\zeta,\eta)$ is treated as a column vector. Denote vector inner product by $< \cdot, \cdot >$.

3 METHOD

Our analysis consists of four stages: extracting streamlines, classifying flower images into early and late periods, identifying a latent category of abstract style within the late period, and explaining the roles of streamline features for identifying abstract images. The following subsections elaborate on each stage.

3.1 Streamline Extraction

Streamline extraction relies on the structure tensor, whose orientation estimates are most stable when computed on a single, coherent intensity field. Converting the RGB image to a grayscale brightness image reduces channel-specific artifacts, suppresses chromatic variations, and yields smoother, geometry-focused gradients. This allows the tensor eigenvectors to reflect underlying structural flow rather than color transitions, resulting in more reliable and visually interpretable streamlines. In Monet's *Water Lilies*, hue and saturation vary within a relatively narrow range, making brightness a natural and robust choice for constructing the grayscale field. For applications to other paintings or image collections, alternative color-to-intensity conversion schemes may be appropriate and can be explored by future users of the method.

We then compute the structure tensor $J(\zeta, \eta)$ at each pixel, from which we derive the directional fields $\{\mathbf{u}_2(\zeta, \eta)\} \mid \zeta = 1, \ldots, n_w;\ \eta = 1, \ldots, n_h\}$. The *Streamline Extraction Algorithm (SEA)* consists of the following steps.

1) Initialize a validity mask containing Boolean values: $\mathcal{M} = (B(\zeta, \eta))_{\zeta=1,\ldots,n_w,\eta=1,\ldots,n_h}$. Set $B(\zeta, \eta)) = T$ ("True") if pixel (ζ, η) belongs to the segmented flower regions; otherwise, set $B(\zeta, \eta)) = F$ ("False").
2) Randomly select a seed point for which $B(\zeta, \eta) = T$ and trace a potential streamline passing through this point using the *Single Streamline Tracing (SST)* algorithm (described below).
3) Update the validity mask $\mathcal{M}$ by setting $B(\zeta, \eta) = F$ for any pixel (ζ, η) lying on the previously identified streamline or within its surrounding 3×3 neighborhood (i.e., all pixels within one-pixel offset in any direction).
4) Repeat Step (2) until no pixel in $\mathcal{M}$ satisfies $B(\zeta, \eta) = T$.
5) To finalize the selection of valid streamlines, count the number of pixels along each streamline and discard those that are too short. Extremely short streamlines——often artifacts of the algorithm——have negligible visual relevance and lack sufficient pixels to support reliable computation of the geometric features defined below. In our experiments, we set the pixel-count threshold to $\max(15, \sqrt{n_w \times n_h}/30)$.

We now describe the SST algorithm for identifying an individual streamline.

1) Trace a streamline by randomly selecting a starting point, say (ζ_0, η_0) within the validity mask $\mathcal{M}$. Compute the eigenvector $\mathbf{u}_2(\zeta_0, \eta_0)$ and set the *initial flow direction* to $\mathbf{u}_f(\zeta_0, \eta_0) = \mathbf{u}_2(\zeta_0, \eta_0)$. Initialize the step counter $n = 1$.
2) Compute the next pixel position (ζ_n, η_n):

$$(\zeta_n, \eta_n)^t = (\zeta_{n-1}, \eta_{n-1})^t + \alpha \cdot \mathbf{u}_f(\zeta_{n-1}, \eta_{n-1}) \ .$$

where the step size is set to $\alpha = 1$.

3) Calculate the *previous flow direction* $\hat{\mathbf{d}}(\zeta_n, \eta_n)$ as the normalized vector between the two most recent positions:

$$\hat{\mathbf{d}}(\zeta_n, \eta_n) = \frac{(\zeta_n - \zeta_{n-1}, \eta_n - \eta_{n-1})^t}{\sqrt{(\zeta_n - \zeta_{n-1})^2 + (\eta_n - \eta_{n-1})^2}} \ .$$

Compute the local eigenvector $\mathbf{u}_2(\zeta_n, \eta_n)$, and let $\xi'_n = \langle \mathbf{u}_2(\zeta_n, \eta_n), \hat{\mathbf{d}}(\zeta_n, \eta_n) \rangle$. Set the updated flow direction:

$$\mathbf{u}_f(\zeta_n, \eta_n) = \begin{cases} \mathbf{u}_2(\zeta_n, \eta_n), & \xi'_n > 0 \\ -\mathbf{u}_2(\zeta_n, \eta_n), & \text{otherwise} \end{cases}$$

By examining the sign of ξ'_n, we ensure that the flow direction extends the streamline forward. Define the *alignment score* ξ_n as

$$\xi_n = |\xi'_n| = \langle \mathbf{u}_f(\zeta_n, \eta_n), \hat{\mathbf{d}}(\zeta_n, \eta_n) \rangle \ ,$$

which increases as the flow direction $\mathbf{u}_f(\zeta_n, \eta_n)$ becomes more aligned with the previous motion (i.e., forming a smaller angle with $\hat{\mathbf{d}}(\zeta_n, \eta_n)$). In addition, compute the eigen-ratio at the current location:

$$\kappa(\zeta_n, \eta_n) = \frac{\lambda_2(\zeta_n, \eta_n)}{\lambda_1(\zeta_n, \eta_n)} \ .$$

4) Continue growing the streamline by repeating Step (2) until one of the following stopping conditions is met:
    a) The alignment score $\xi_n \le \tau$.
    b) $\kappa(\zeta_n, \eta_n) \ge \omega$.
    c) The new pixel falls outside the validity mask $\mathcal{M}$, i.e., $B(\zeta_n, \eta_n) = F$).

    In our experiments, we set the thresholds to $\tau = 0.7$ and $\omega = 0.5$. The rationale behind these conditions will be discussed shortly.
5) After tracing in the initial direction, extend the streamline starting from (ζ_0, η_0) in the *opposite* direction of $\mathbf{u}_2(\zeta_0, \eta_0)$, that is, let $\mathbf{u}_f(\zeta_0, \eta_0) = -\mathbf{u}_2(\zeta_0, \eta_0)$. Repeat Steps (2)–(4).
6) Let the two traced sequences be $\{(\zeta_0, \eta_0), (\zeta_1, \eta_1), ..., (\zeta_{n_1}, \eta_{n_1})\}$ and $\{(\zeta_0, \eta_0), (\zeta'_1, \eta'_1), ..., (\zeta'_{n_2}, \eta'_{n_2})\}$. Construct the final streamline by reversing the second traced sequence and concatenating it with the first:

$$\{(\zeta'_{n_2}, \eta'_{n_2}), (\zeta'_{n_2-1}, \eta'_{n_2-1}), ..., (\zeta'_1, \eta'_1), \\ (\zeta_0, \eta_0), (\zeta_1, \eta_1), ..., (\zeta_{n_1}, \eta_{n_1})\} \ .$$

The validity mask $\mathcal{M}$ is used in Step (4) to determine whether a streamline should continue extending. By restricting growth within $\mathcal{M}$, we prevent new streamlines from intersecting and duplicating segments of existing ones. We also require $\xi_n > \tau$ to proceed with extension, ensuring that the direction between consecutive growth steps does not change abruptly. This condition promotes smooth and natural-looking streamlines. Lastly, the constraint $\kappa(\zeta_n, \eta_n) < \omega$ ensures that the streamline continues only where the flow remains visually coherent, effectively preventing incorrect extensions—such as when the meaningful trajectory of the streamline has already ended.

The number of streamlines per image ranges from 2 to 1292, with a mean of 143 and a standard deviation of 206. For each streamline specified by an ordered sequence of pixels: $\{(\zeta_i, \eta_i)\}_{i=0}^{n}$, we compute a sequence of turning angles θ_i that capture the curvature. For every pixel (ζ_i, η_i) used as a central point, and with a fixed positional lag δ (set to 3), we compute two direction vectors:

$$\begin{aligned}\mathbf{a} &= (\zeta_i, \eta_i)^t - (\zeta_{i-\delta}, \eta_{i-\delta})^t \ , \\ \mathbf{b} &= (\zeta_{i+\delta}, \eta_{i+\delta})^t - (\zeta_i, \eta_i)^t \ .\end{aligned}$$

The *turning angle* θ_i at (ζ_i, η_i), for $i = \delta, ..., n-\delta$, is defined as:

$$\theta_i = \arccos\left(\frac{\mathbf{a}\cdot\mathbf{b}}{\|\mathbf{a}\|\,\|\mathbf{b}\|}\right) \ ,$$

where $\|\cdot\|$ denotes L_2 norm. θ_i quantifies the local directional change of the streamline at each point. We further define the *absolute turning angle change* $\Delta\theta_i = |\theta_i - \theta_{i-1}|$, for $i = 1, ..., n$.

Based on the sequences θ_i and $\Delta\theta_i$, we define 11 features grouped into five categories, each capturing a distinct geometric characteristics of the streamline. Detailed descriptions of these features are provided in Supplementary Materials.

1) Curvature: $\{\theta_{\text{ave}}, \theta_{\text{min}}, \theta_{\text{max}}\}$, referred to as *average curvature*, *minimum curvature*, and *maximum curvature*, respectively.
2) Variation in curvature: $\{\sigma_\theta^2, H_\theta\}$, referred to as *variance of curvature* and *entropy of curvature*, respectively.
3) Length: $\{L_{\text{norm}}, L_{\text{seg,norm}}\}$, referred to as *normalized streamline length* (or simply as length) and *length of the longest smooth segment*, respectively.
4) Level of wiggliness (i.e., the degree of oscillatory behavior): $\{\Delta\theta_{\text{max}}, \Delta\theta_{\text{ave}}, V_c\}$ referred to as *maximum curvature change*, *average turning angle change*, and *average curvature change*, respectively.
5) Second-order variation of curvature (i.e., the variability in the degree of oscillation): $\sigma_{\Delta\theta}^2$ referred to as *variance of curvature change*.

3.2 C2A Neural Network for Distributional Data

Consider a labelled dataset, $\{(\mathbf{x}_i, Y_i)\}_{i=1}^{N}$, $Y_i \in \{0, 1, \ldots, K-1\}$, where N is the number of instances and K the number of classes. Each instance $\mathbf{x}_i = \{x_j^{(i)}\}_{j=1}^{n_i}$, $x_j^{(i)} \in \mathbb{R}^d$, is a **set** (no ordering) of d-dimensional feature vectors whose cardinality n_i may vary across instances. We regard $\mathbf{x}_i$ as an empirical (discrete uniform) distribution supported on the elements $x_j^{(i)}$ and therefore call it *distributional* data. In the context of Monet analysis, each instance $\mathbf{x}_i$ corresponds to a flower-patch image extracted from a painting, and each element $x_j^{(i)}$ denotes an individual streamline within that patch.

The architecture of the neural network *Composition to Attribute (C2A)* is illustrated in Fig. 2. C2A operates in two stages: element-level clustering and instance-level classification. The clustering stage processes individual elements within each instance—in our context, streamlines—and can adopt any classifier architecture. In our implementation, we use a multilayer perceptron (MLP) with one hidden layer. However, unlike a conventional classifier, this stage is not trained with ground-truth labels. Instead, its parameters are optimized jointly as part of the end-to-end training of C2A. Supervision is provided only at the instance level, with class labels used in the objective function to guide the subsequent classification stage. Because the clustering module does not receive direct supervision at the element level, it functions as an unsupervised classifier— hence the term "clustering." The output of this stage is a set of posterior probabilities indicating each streamline's membership in a cluster. We refer to these clusters as *latent streamline classes (LS-classes)*.

As shown in Fig. 2, C2A consists of four main modules: the *Feature Extraction Module (FEM)*, *Clustering Module (CLUM)*, *Aggregation Module (AM)*, and *Classification Module (CLAM)*, denoted respectively by G_f, G_u, G_a, and G_c. The mathematical operations carried out by each of these modules within the C2A pipeline are described below.

1) For each $x_j^{(i)}$, $j = 1, ..., n_i$, $i = 1, ..., N$, let $\tilde{x}_j^{(i)} = G_f(x_j^{(i)})$.
2) Apply G_u to each $\tilde{x}_j^{(i)}$ and obtain posterior over K LS-classes: $p_{i,j,k}$, $k = 1, ..., K$, $j = 1, ..., n_i$, $i = 1, ..., N$. Note that $\sum_k p_{i,j,k} = 1$. Let $\mathbf{p}_{i,j} = (p_{i,j,1}, ..., p_{i,j,K})^t$ and $\mathbf{p}_i = (\mathbf{p}_{i,1}, \mathbf{p}_{i,2}, ..., \mathbf{p}_{i,n_i})$.
3) Apply $G_a(\mathbf{x}_i, \mathbf{p}_i)$, $i = 1, ..., N$, to obtain the following attributes:
    a) Overall average of features: $\overline{\mathbf{x}}_i = \dfrac{1}{n_i}\sum_{j=1}^{n_i} \tilde{x}_j^{(i)}$.
    b) Proportions of LS-classes for each instance $\mathbf{x}_i$: $\overline{\mathbf{p}}_i = \dfrac{1}{n_i}\sum_{j=1}^{n_i} \mathbf{p}_{i,j}$.
    c) Average feature vectors for each LS-class: $\boldsymbol{\mu}_{i,k}$, $i = 1, ..., N$, $k = 1, ..., K$:
    $$\boldsymbol{\mu}_{i,k} = \frac{\sum_{j=1}^{n_j} p_{i,j,k}\tilde{x}_j^{(i)}}{\sum_{j=1}^{n_j} p_{i,j,k}} \ .$$
    d) We then concatenate the elements of $\overline{\mathbf{x}}_i$, $\overline{\mathbf{p}}_i$, and $\boldsymbol{\mu}_{i,k}$ for $k = 1, \ldots, K$ into a single attribute vector, denoted by $\mathbf{v}_i$. The resulting set of training pairs of attribute vectors and class labels, $\{(\mathbf{v}_i, Y_i)\}_{i=1}^{N}$, is used to train the classification module G_c.

Except for the aggregation module G_a, which is predefined, the remaining three modules—G_f, G_u, and G_c—are jointly optimized via end-to-end training. The final loss function is defined as the cross-entropy between the predicted labels $\hat{Y}_i$ and the ground truth labels Y_i. We refer to the components in $\mathbf{v}_i$ as *attributes*, which represent holistic image-level information and serve as inputs to the classification module G_c. In contrast, the outputs of G_f, which are computed for individual streamlines, are referred to as *features*.

We experimented with several architectural configurations. As described above, the aggregation module G_a produces three types of attributes: (1) the average feature vector across all streamlines in an image; (2) the proportions of streamlines assigned to each LS-class; and (3) the

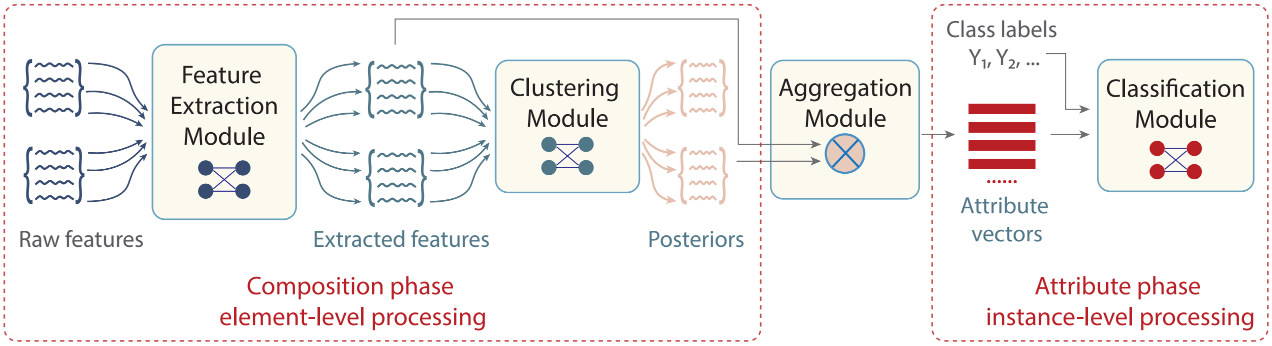

Fig. 2. Architecture of the C2A network.

LS-class–wise average of features within each image. A given configuration may use any combination of these three types—individually, in subsets, or all together—as input to the classification module G_c. As explained in Section 4, the configuration used for analyzing Monet's flower patches relies solely on the average feature vector. Consequently, in the following discussion, the attributes correspond to the average features and are referred to simply as features.

3.3 DEGA: Discover Embedded Group with Asymmetry

Art historians' interest in Monet's *Water Lilies* extends beyond distinguishing between his early and late periods. Rather, they have speculated that Monet developed a distinct stylistic approach to depicting water lilies during the latter years of his career that influenced practitioners of abstract art in the middle of the twentieth century [31]. Yet, identifying the defining characteristics of this emergent style remains challenging. While some have described this late style as "abstract," the precise meaning of abstraction in art differs according to context [32]. In the absence of a widely accepted term, we provisionally adopt the label "abstract," while acknowledging that a central aim of our analysis is to clarify what this term entails in the context of Monet's output.

To investigate this, we formulate two hypotheses to uncover the meaning of abstractness, to identify images that embody it, and to derive quantitative measures of its distinctiveness. First, we posit that an abstract style is represented in a subset of flower patches painted during Monet's late period—a premise that is broadly shared among art historians. Second, we assume that the features distinguishing this subgroup from others do not generalize to a broader separation between the early and late periods outside of the subgroup. Since the abstract type is treated as a latent class, the second assumption is critical: it ensures that a genuinely distinct subgroup, rather than a trivial partition aligned with chronology, can be discovered.

Modeling a latent abstract subgroup without ground-truth labels presents a dilemma, especially given the complexity and subtlety of the data. To address this, we employ the C2A Network—a DNN—to model and distinguish the abstract subgroup. However, DNNs are prone to overfitting, and without labeled data for the latent class, it is particularly difficult to differentiate meaningful patterns from non-generalizable ones. The second assumption, implemented as a regularization term in C2A, helps mitigate this risk by suppressing spurious patterns.

We introduce a framework, *Discover Embedded Groups with Asymmetry (DEGA)*, to identify this latent abstract subgroup. Under the two hypotheses, DEGA seeks to discover a group of flower patches that is distinguishable from other images based on extracted features, while patches outside the group—regardless of period—remain indistinguishable. To better interpret the latent abstract subgroup, we prioritize the use of interpretable features, and examine multiple strategies for gaining insight into their underlying meaning.

The first step of DEGA is to estimate the proportion of images from the late period that belong to the abstract subgroup. Let $\mathcal{S}_e$ denote the set of instances from the early period (i.e., $Y = 0$) and $\mathcal{S}_l$ denote those from the late period (i.e., $Y = 1$). Define the abstract subgroup by $\mathcal{E}$, which relates to $\mathcal{S}_e$ and $\mathcal{S}_l$ asymmetrically: $\mathcal{E} \subset \mathcal{S}_l$ and $\mathcal{E} \cap \mathcal{S}_e = \emptyset$. Let Z indicate membership in $\mathcal{E}$, with $Z = 1$ for instances in $\mathcal{E}$ and $Z = 0$ otherwise. The proportion of abstract instances among those in the late period is denoted by γ, where $\gamma = |\mathcal{E}|/|\mathcal{S}_l|$.

We assume the existence of a strong classifier that can reliably distinguish instances with $Z = 1$ from those with $Z = 0$. However, instances with $Y = 0$ and those with $Y = 1$ and $Z = 0$ are assumed to be statistically indistinguishable. Under this assumption, a classifier trained to predict Y effectively identifies the abstract subgroup $\mathcal{E}$ (i.e., $Z = 1$), while being unable to separate the remaining instances. Consequently, as we demonstrate later, the classification performance on Y—specifically its true negative rate and false negative rate—can be leveraged to estimate the proportion γ of abstract instances within the late period.

However, due to the strong tendency of DNNs to overfit, evaluating performance on the training set is unreliable. Given the relatively small dataset, we adopt a cross-validation strategy referred to as *leave-one-painting-out cross-validation (LOPO-CV)*. In contrast to standard cross-validation, LOPO-CV assigns all patches from the same painting to a single test fold, thereby avoiding inflated accuracy estimates that may arise from visual similarity among patches within the same painting. As demonstrated in our experiments, LOPO-CV consistently yields more conservative yet realistic accuracy estimates than standard cross-validation protocols.

Suppose a classifier can reliably distinguish instances with $Z = 1$ from those with $Y = 0$, while any apparent separation between $Y = 0$ and $Y = 1$, $Z = 0$ is merely an artifact of overfitting, which we model as random guessing. Specifically, for any instance with $Y = 0$ or with $Y = 1$ and $Z = 0$, the classifier outputs $\hat{Y} = 0$ with probability p and $\hat{Y} = 1$ with probability $1 - p$. That is,

$$P(\hat{Y} = 0 \mid Y = 0) = P(\hat{Y} = 0 \mid Y = 1,\, Z = 0) = p\,.$$

Suppose that the prior probability for $Y = 0$ is q and for $Y = 1$ is $1 - q$. We can now compute $P(Y = 1, \hat{Y} = 0)$ in two ways:

$$\begin{aligned} & P(Y = 1, \hat{Y} = 0) \\ = \; & P(Y = 1)P(\hat{Y} = 0|Y = 1) \\ = \; & (1 - q) \cdot P(\hat{Y} = 0|Y = 1)\,, \end{aligned}$$

$$\begin{aligned} & P(Y = 1, \hat{Y} = 0) \\ = \; & P(Y = 1, Z = 0, \hat{Y} = 0) + P(Y = 1, Z = 1, \hat{Y} = 0) \\ = \; & P(Y = 1)P(Z = 0|Y = 1)P(\hat{Y} = 0|Y = 1, Z = 0) \\ & + P(Y = 1)P(Z = 1|Y = 1)P(\hat{Y} = 0|Y = 1, Z = 1) \\ = \; & (1 - q)(1 - \gamma)p + (1 - q)\gamma \cdot 0 \\ = \; & (1 - q)(1 - \gamma)p\,. \end{aligned}$$

Thus

$$\gamma = 1 - \frac{P(\hat{Y} = 0|Y = 1)}{P(\hat{Y} = 0|Y = 0)}\,. \tag{2}$$

We use this equation to estimate γ, where both $P(\hat{Y} = 0 \mid Y = 0)$ and $P(\hat{Y} = 0 \mid Y = 1)$ are computed from the LOPO-CV results of the C2A neural network.

Once γ is estimated, we retrain a C2A network using the same architecture and hyperparameters as in the original $Y = 0$ versus $Y = 1$ classification task. However, instead of the standard cross-entropy loss, we employ a modified loss function defined as:

$$\mathcal{L}_{\text{DEGA}} := \mathcal{L}_{\text{CE}} + \mathcal{L}_{\text{R}}\,,$$

where $\mathcal{L}_{\text{CE}}$ is the binary cross-entropy loss for label Z.

Because Z is a latent class label, it is initially estimated based on the predictions of the C2A classifier trained to distinguish Y, and subsequently updated during our iterative procedure. Details of this process will be described later.

The regularization loss $\mathcal{L}_{\text{R}}$ is defined as a weighted combination of two components:

$$\mathcal{L}_{\text{R}} := \lambda_1 \mathcal{L}_{\text{W}} + \lambda_2 \mathcal{L}_{\text{B}}\,.$$

The regularization term $\mathcal{L}_{\text{R}}$ encourages the extracted features to exhibit specific desired properties. In particular, $\mathcal{L}_{\text{W}}$ measures the difference between the average features of non-abstract patches from the two time periods, promoting temporal consistency. A smaller $\mathcal{L}_{\text{W}}$ indicates that non-abstract patches from the early and late periods share similar feature representations. On the other hand, $\mathcal{L}_{\text{B}}$ quantifies the overlap between the feature distributions of abstract and non-abstract patches, encouraging class separability. A smaller $\mathcal{L}_{\text{B}}$ reflects stronger distinction between abstract and non-abstract features. Fig. 3 illustrates the respective effects of the three loss components. In essence, $\mathcal{L}_{\text{B}}$ promotes separation between abstract and non-abstract patches, while $\mathcal{L}_{\text{W}}$ promotes alignment between non-abstract patches across time periods.

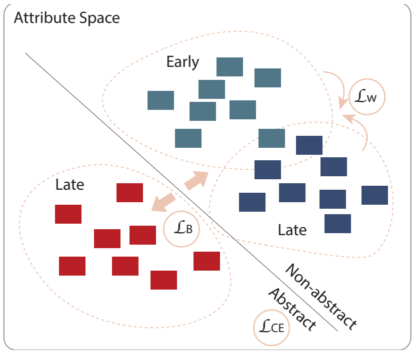

Fig. 3. Illustration of the effects of the three types of loss functions used by DEGA to train the C2A network.

Let the extracted average feature vector for image i be denoted by $\mathbf{v}_i \in \mathbb{R}^{d'}$, for $i = 1, \ldots, N$, where d' is the dimensionality of the feature space. Recall that each feature vector $\mathbf{v}_i$ is associated with two labels: Y_i, indicating the time period ($Y_i = 0$ for the early period and $Y_i = 1$ for the late period), and Z_i, indicating whether the flower is painted in an abstract style ($Z_i = 1$) or a non-abstract style ($Z_i = 0$). Define the index sets $\mathcal{Y}_j = \{i : Y_i = j\}$ for $j = 0, 1$, and $\mathcal{Z}_j = \{i : Z_i = j\}$ for $j = 0, 1$. For example, $\mathcal{Y}_0$ contains the indices of patches from the early period, i.e., those with $Y_i = 0$.

We compute the sample standard deviation for each feature dimension across instances in each subgroup defined by $Z_i = 0$ and $Z_i = 1$. Let $\boldsymbol{\sigma}_j = (\sigma_{j,1}, \ldots, \sigma_{j,d'})^t$ denote the vector of standard deviations for group $Z_i = j$, with $j = 0, 1$. Define the average standard deviation vector as $\overline{\boldsymbol{\sigma}} = (\boldsymbol{\sigma}_0 + \boldsymbol{\sigma}_1)/2$.

Define the following average features: $\overline{\mathbf{v}}_{0,0} = \sum_{i \in \mathcal{Y}_0 \cap \mathcal{Z}_0} \mathbf{v}_i / |\mathcal{Y}_0 \cap \mathcal{Z}_0|$, $\overline{\mathbf{v}}_{1,0} = \sum_{i \in \mathcal{Y}_1 \cap \mathcal{Z}_0} \mathbf{v}_i / |\mathcal{Y}_1 \cap \mathcal{Z}_0|$, $\overline{\mathbf{v}}_{\cdot,0} = (\overline{\mathbf{v}}_{0,0} + \overline{\mathbf{v}}_{0,1})/2$, and $\overline{\mathbf{v}}_{\cdot,1} = \sum_{i \in \mathcal{Z}_1} \mathbf{v}_i / |\mathcal{Z}_1|$. Note that $Y = 0$ implies $Z = 0$, and thus $\mathcal{Y}_0 \cap \mathcal{Z}_0 = \mathcal{Y}_0$. We scale the following average feature vectors by the standard deviation vector $\boldsymbol{\sigma}_0$, applying the division element-wise: $\overline{\mathbf{v}}'_{0,0} = \overline{\mathbf{v}}_{0,0}/\boldsymbol{\sigma}_0$, $\overline{\mathbf{v}}'_{1,0} = \overline{\mathbf{v}}_{1,0}/\boldsymbol{\sigma}_0$, $\overline{\mathbf{v}}'_{\cdot,0} = \overline{\mathbf{v}}_{\cdot,0}/\boldsymbol{\sigma}_0$, where $\overline{\mathbf{v}}_{j,0}$ denotes the mean feature vector of instances with $Y = j$ and $Z = 0$, and $\overline{\mathbf{v}}_{\cdot,0}$ denotes the overall mean feature vector of all instances with $Z = 0$. We then define

$$\mathcal{L}_{\text{W}} := \frac{1}{2}\left(\|\overline{\mathbf{v}}'_{0,0} - \overline{\mathbf{v}}'_{\cdot,0}\| + \|\overline{\mathbf{v}}'_{1,0} - \overline{\mathbf{v}}'_{\cdot,0}\|\right)\,.$$

To measure the relative tightness of the extracted features within the groups $\mathcal{Z}_0$ and $\mathcal{Z}_1$, we define a d'-dimensional vector $\boldsymbol{r} = (r_1, r_2, \ldots, r_{d'})^t$: $\boldsymbol{r} = \dfrac{\overline{\boldsymbol{\sigma}}}{|\overline{\mathbf{v}}_{\cdot,1} - \overline{\mathbf{v}}_{\cdot,0}|}$, where both the absolute value function and the division are applied element-wise. A smaller value of r_j indicates tighter groups. Finally, we define:

$$\mathcal{L}_{\text{B}} := \min_{j=1,\ldots,d'} r_j\,.$$

Because the Z_i's are estimated, we update their estimation iteratively when optimizing the DEGA network. Denote the C2A model trained for classifying time periods Y by $\mathcal{M}_{\mathrm{Y}}$ and the model to be trained by DEGA by $\mathcal{M}_{\mathrm{Z}}$. In summary, the DEGA algorithm entails the following steps:

1) Initialize $\mathcal{M}_{\mathrm{Z}}$ using $\mathcal{M}_{\mathrm{Y}}$.
2) Identify $100 \cdot \gamma\%$ of the images that have the highest posterior probability of being in Class 1 based on $\mathcal{M}_{\mathrm{Z}}$ and assign $Z = 1$ to those images.
3) Retrain $\mathcal{M}_{\mathrm{Z}}$ using the Z labels and the loss function $\mathcal{L}_{\mathrm{CE}}$.
4) Repeat Steps (2) and (3) k_1 times, where k_1 is set to 6 in our implementation.
5) Switch to the loss function $\mathcal{L}_{\mathrm{DEGA}}$ and repeat Steps (2) and (3) k_2 times, with k_2 set to 3.

The loss $\mathcal{L}_{\mathrm{CE}}$ is first used to obtain an accurate estimate of Z, followed by several additional training rounds with $\mathcal{L}_{\mathrm{DEGA}}$ to derive features exhibiting the desired properties.

3.4 Interpreting Learning Outcomes

As will be explained in detail in Section 4, DEGA discovers a 2-D feature space that represents the patches. This 2-D feature vector of each patch is the average of the features computed from individual streamlines. Both features formed in $\mathcal{M}_{\mathrm{Z}}$ are non-linear. To interpret the features, we employ two approaches. First, we perform linear regression of each feature using the original streamline geometric features. Linear regression allows us to examine the coefficients of the input variables, which directly indicate the contribution of each geometric feature. This regression-based interpretation provides global insight. However, the accuracy of the linear model is limited, so any interpretation derived from it must be treated with caution.

To address this limitation, we adopt a second approach based on decision trees. In this framework, a decision tree is trained to distinguish between groups formed by partitioning the range of an extracted feature into discrete intervals, which we refer to as *feature categories*. This method is inherently interpretable: each leaf node in the tree corresponds to a conjunction of simple decision rules—comparisons between feature values and thresholds—making the resulting model transparent and easy to understand. When the estimated probability of a particular feature category at a leaf node approaches 1, it indicates that the corresponding region in feature space is overwhelmingly dominated by that category. We refer to such highly decisive regions as *Assertive Regions (AR)*. These ARs highlight specific combinations of feature values under which an instance can be assigned to a given category with high confidence. By isolating and examining these regions, we gain insight into the structural patterns that drive classification and uncover interpretable, high-probability conditions for membership in each category.

We define two criteria for identifying an AR: (1) the region must exhibit high purity, meaning that the predicted probability of the dominant class exceeds a predefined threshold τ (set to 0.9 in our implementation); and (2) it must contain a sufficiently large fraction of data points—specifically, at least 5% of the total instances belonging to the dominant category. These two conditions reflect key principles of interpretable modeling: high certainty (confidence in prediction) and broad applicability (coverage across the population). Because ARs are constructed from the leaf nodes of a decision tree, they are also readily interpretable, with their boundaries defined by a transparent sequence of feature-based rules. However, one limitation is that the proportion of data falling into ARs cannot be predetermined or directly controlled. As a result, the interpretability and insight provided by ARs apply only to a subset of the data, leaving some instances outside the scope of this high-certainty explanatory framework.

4 EXPERIMENTS

4.1 Findings from Classifying Time Periods Using C2A

We experimented with multiple architectural configurations of the C2A model, determined by two hyperparameters: d' (the dimensionality of the extracted features) and K (the number of LS-classes). Specifically, we considered $d' = 2, 3, 4$ and $K = 1, 2, 4$. When $K = 1$, only the average of the extracted feature vectors across an entire image is used as the input attributes to the CLAM component G_c. When $K > 1$, the input attributes include both the average extracted features and the proportions of streamlines assigned to each LS-class within an image.

The three modules—G_f (FEM), G_u (CLUM), and G_c (CLAM)—are implemented as multi-layer perceptrons (MLPs). G_f consists of a single hidden layer with d nodes, where d is the dimension of the original streamline feature vector; G_u includes two hidden layers with d and K nodes, respectively; G_c has one hidden layer with $4(d' + K)$ nodes. For brevity, we refer to each architectural configuration by the pair (d', K) in the discussion below.

In addition, when multiple LS-classes are present, we address the heterogeneity among the feature components (cluster proportions and mean extracted features) by employing a lightweight Transformer-based attention head, inspired by the FT-Transformer architecture [33], for G_c. Each scalar feature is first linearly projected into a shared embedding space of dimension $d_t = 16$, forming a short sequence of feature tokens. The sequence, augmented with a learnable summary token that aggregates global information, is passed through a Transformer block with two attention heads, a feed-forward expansion ratio of 2, and a dropout rate of 0.1. The output corresponding to the summary token is used as the global representation for classification. This compact attention head enables adaptive reweighting and interaction among heterogeneous feature types while maintaining low model complexity, which is appropriate for the scale of the painting dataset. The hyperparameters ($d_t = 16$, two attention heads, and one block depth) were selected to balance expressiveness and generalization given the moderate feature dimensionality (< 20) and limited sample size (< 600).

Fig. 4(a) presents boxplots of classification accuracy evaluated using LOPO-CV, with each configuration repeated multiple times to capture variability arising from the stochastic nature of C2A training. Possibly due to the limited sample size, when G_c is implemented as an MLP, C2A tends to perform better with smaller values of d' and K. For $K > 1$, however, using a Transformer model for G_c consistently yields higher accuracy than the MLP. The boxplots are color-coded by the value of d'. Under the Transformer G_c, models with $d' = 2$ or 3 achieve comparable accuracy. The two best configurations, based on median accuracy, are the Transformer G_c with $(d', K) = (2, 4)$ and $(3, 4)$. Nonetheless, relative to the configuration $(d', K) = (2, 1)$ with an MLP G_c, the median improvement is modest (approximately 2.5%), and the best individual accuracy from $(2, 1)$ exceeds the median of the top-performing Transformer-based models. These results indicate an advantage in incorporating multiple LS-classes, although the gain is modest for this dataset. Given that the configuration $(d', K) = (2, 1)$ yields a more interpretable model with substantially lower-dimensional extracted features, we adopt it for subsequent analysis. Nevertheless, evaluating the more complex configurations is valuable, as it confirms that the chosen configuration attains satisfactory accuracy. To estimate γ, we examine the four best-performing runs under this configuration. Based on Eq. (2), the estimated γ values range from 35% to 38%, with an average of 37%, which we use in later analysis.

4.2 Identifying the Abstract Class by DEGA

TABLE 1
Paintings containing abstract patches. For each painting, the numbers of abstract, non-abstract, and quasi-abstract patches are listed.

Painting ID	Year	Abstract	Non-abstract	Quasi-abstract
15	1922	13	1	1
11	1916	12	1	0
13	1914-17	10	7	7
48	1914-15	9	2	1
58	1916-19	5	0	0
23	1914-17	4	3	0
59	1916-19	4	1	0
16	1918	4	5	0
62	1919	4	3	0
67	1914-17	3	6	0
19	1917-19	3	11	0
25	1920-26	3	13	0
22	1914-17	1	7	0
50	1915-17	1	16	0
9	1916-19	1	11	0
37	1916	1	10	0
56	1916-19	1	2	1
64	1916-19	1	2	0
63	1919	1	11	0

DEGA is applied to train a model $\mathcal{M}_Z$ that classifies patches as either $Z = 1$ (abstract) or $Z = 0$ (non-abstract), where Z denotes membership in the abstract class. A total of 81 patches are identified as abstract ($Z = 1$). Among the 47 paintings analyzed, 24 belong to the late period. As summarized in Table 1, 65 of the 81 abstract patches originate from just 9 late-period paintings. Within these 9 paintings, the proportion of abstract patches in each painting ranges from 44% to 100%, with a median of 80%. An additional 10 late paintings contain only a few abstract patches—7 of them containing exactly one. Given the inherent limitations of our learning algorithm, it is plausible that the isolated detection of a single abstract patch amidst many non-abstract ones within the same painting may reflect model imperfection rather than genuine stylistic presence.

Overall, these findings suggest that abstract-style patches are not randomly distributed but tend to appear in concentrated form within a subset of late-period paintings. This indicates that the abstract style is not a sporadic occurrence but rather a deliberate and consistent artistic choice employed in certain works. The results identify a coherent sub-set of work in terms of time period, thus according with qualitative assessments of Monet's art that identify a shift in the artist's rendering of the water lily pond towards the end of the First World War. As Monet began to execute or plan for his final large-scale decorative works, his palette and brushwork combined to create paintings that simply "suggested" the presence of water lilies and their pads floating on the surface of the pond [34]. Yet the results also reveal that Monet experimented over a longer period with the reduction of optical information into painted marks that bear an isomorphic relation to real water lilies without rendering their actual visual structure.

Subsequent analysis of the two features extracted by DEGA further supports the introduction of a quasi-abstract category: patches labeled as non-abstract ($Z = 0$) but exhibiting strong similarity to the abstract class. The precise definition of the quasi-abstract subclass will be provided in the next subsection. Only 2.7% of patches meet this criterion. Notably, all three quasi-abstract patches from the early period are close-up flower paintings, which, by design, are treated as non-abstract. To distinguish these visually similar early-period patches from true abstract patches, $\mathcal{M}_Z$ also assigns the non-abstract label to a few comparable late-period patches. A more detailed discussion of this trade-off will follow.

As shown in Table 1, the most notable paintings characterized by predominantly abstract or quasi-abstract patches include those with IDs 15, 11, 13, 48, 58, and 59. In these paintings, all patches are abstract or quasi-abstract—except in paintings 11, 48, and 59, each of which contains a single strongly non-abstract patch (i.e., labeled non-abstract and not quasi-abstract). Notably, most quasi-abstract patches come from paintings dominated by abstract flower patches. The distinction between quasi-abstract and abstract arises because the former resemble close-up flower patches in Monet's earlier period.

To further ensure that the patches labeled with $Z = 1$ by DEGA reflect a meaningful and distinctive style rather than an artifact of overfitting in $\mathcal{M}_Z$, we compared the classification performance of the C2A network using DEGA-generated Z labels against two alternative labeling schemes. In the first scheme, referred to as "Random late period," we assigned $Z = 1$ to 81 randomly selected patches from the late period and $Z = 0$ to all remaining patches from both periods. Multiple label sets were generated under this random scheme. The number 81 matches the proportion $\gamma = 37\%$ inferred by DEGA (i.e., DEGA also identifies 81 late-period patches as having $Z = 1$). Because no authoritative human-provided labels for Z exist, we constructed a more challenging comparison. In the second scheme, referred to as "Selected paintings," we assigned $Z = 1$ to all flower patches from the eight paintings that DEGA identified as containing the largest numbers of abstract patches. These paintings (the top eight entries in Table 1) contain a total of 81 patches, of which 61 overlap with the DEGA-generated $Z = 1$ set.

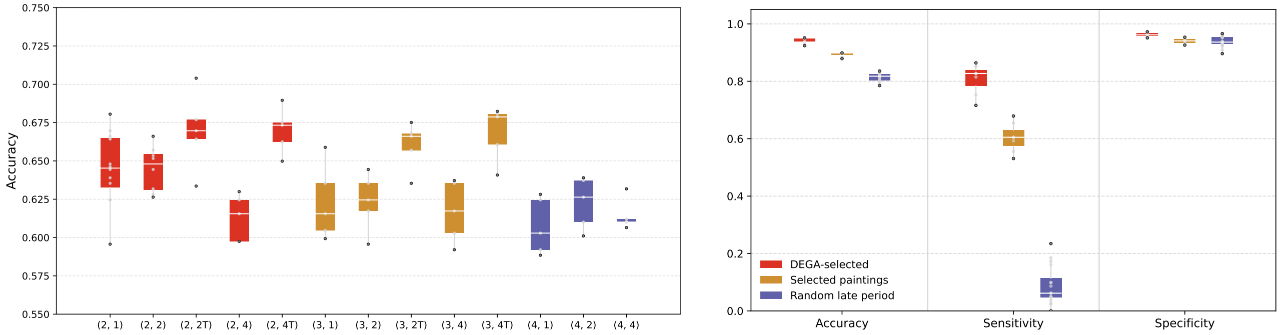

(a) (b)

Fig. 4. Classification performance of the C2A network under different experimental setups. All metrics are obtained using the LOPO-CV protocol. (a) Boxplots showing classification accuracy for distinguishing early versus late periods. Each boxplot corresponds to a specific structural configuration of the C2A network, determined by the hyperparameters (d', K)—the dimensionality of the extracted features and the number of LS-classes—as indicated on the x-axis labels. When the Transformer model is used as G_c, the corresponding x-axis label is marked with "T". (b) Boxplots of accuracy, sensitivity, and specificity for the C2A network with configuration $(d', K) = (2, 1)$ in the task of classifying abstract ($Z = 1$) versus non-abstract ($Z = 0$) patches. Three sets of Z labels are evaluated. In the first set, Z labels are generated by DEGA ("DEGA-generated"); in the second, Z labels are assigned as 1 for all flower patches in eight selected paintings based on the result of DEGA ("Selected paintings"); in the third, $Z = 1$ is assigned to randomly selected patches from late-period paintings ("Random late period"). These three cases are distinguished by color, as indicated in the legends. Across all three label sets, the same proportion $\gamma = 0.37$ is maintained, that is, 81 late-period flower patches are labeled with $Z = 1$. Overall, 85.4% of all patches in the dataset are labeled as $Z = 0$. The mean performance measures for the three cases, in the order of "DEGA-generated," "Selected paintings," and "Random late period," are as follows: accuracy: $(0.940,\ 0.891,\ 0.814)$; sensitivity: $(0.808,\ 0.603,\ 0.087)$; specificity: $(0.962,\ 0.941,\ 0.938)$.

For both the "DEGA-generated" and "Selected paintings" label schemes, we repeated C2A training multiple times and evaluated performance using LOPO-CV.

In Fig. 4(b), boxplots compare the accuracy, sensitivity, and specificity obtained using DEGA-generated Z labels versus the two alternative label schemes. Classification based on DEGA-generated labels is consistently superior across all metrics. Although the accuracy differences may appear modest due to class imbalance (14.2% with $Z = 1$), the gap in sensitivity is substantial: the median sensitivity for the DEGA-generated labels is close to 85%, whereas for the "Random late period" labels it is about 5%. This extremely low sensitivity indicates that the classifier is effectively defaulting to majority-class prediction rather than learning any meaningful pattern, which is an expected outcome, since these labels contain little informative signal. Even more revealing is the performance under the "Selected paintings" scheme. Although these labels overlap heavily with the DEGA-generated labels, the resulting median sensitivity is only about 60%, considerably lower than that achieved using DEGA-generated labels. The comparison demonstrates that the patches marked with $Z = 1$ by DEGA indeed correspond to a meaningful, coherent, and distinguishable stylistic pattern, one that alternative labeling schemes fail to reproduce.

Furthermore, we obtained a qualitative evaluation of the patches assigned $Z = 1$ by DEGA from an art historian. Acknowledging the longstanding debates surrounding the development of Monet's style, the art historian observed that DEGA isolates painted marks that are highly gestural and suggestive of floral motifs. This accords with a qualitative assessment of the presence of 'abstraction' in Monet's art in the sense of a reduction of information about real objects. Yet it also encourages a wider conception of what abstraction means in this context. Importantly, Monet's *Water Lilies* retained a point of reference in the real world; that is, they remained depictions of the water lily pond and its flora as opposed to becoming a non-referential interplay of form, line, and color. Noting this point, Denis Rouart [35] argues that Monet gradually became a 'tachist' painter (as opposed to an abstract painter). 'Tachisme' was a style of painting that came to the fore in Europe in the 1940s and 1950s and was characterized by spontaneous, often calligraphic brushwork. It is sometimes posited as a European equivalent of American Abstract Expressionism. For Rouart, Monet was the first 'tachist' painter in France [35]. In keeping with this perspective, DEGA identifies water lilies forms that are highly gestural, underscoring the productive tension that Monet created between the representation of actual objects, the assertion of painterly mark-making for its own sake, and a means of depicting the visible world through reduced visual means.

Fig. 5 presents example flower patches categorized as abstract, non-abstract, and quasi-abstract. Notably, the only quasi-abstract patches from the early period are three close-up views of flowers. Contrary to what one might expect, "abstract" does not necessarily imply a sketchy, non-mimetic rendering of a depicted object (in this case, the water lily); rather, it relates more to the expressive qualities of the brushwork—an aspect explored in greater detail in the next subsection. Some abstract patches do appear sketchy, with entire flowers suggested by a single brushstroke, while others depict numerous individual petals with care. Conversely, non-abstract patches can also range from sketchy to anatomically detailed. In Fig. 5(e, f), we include examples of sketchy flower patches from both the abstract and non-abstract classes.

4.3 Deriving Interpretable Features

In the DEGA model $\mathcal{M}_Z$, two nonlinear features, denoted by $\tilde{x}_1^*$ and $\tilde{x}_2^*$, are extracted by G_f (FEM) for each streamline. The averages of these two-dimensional feature vectors

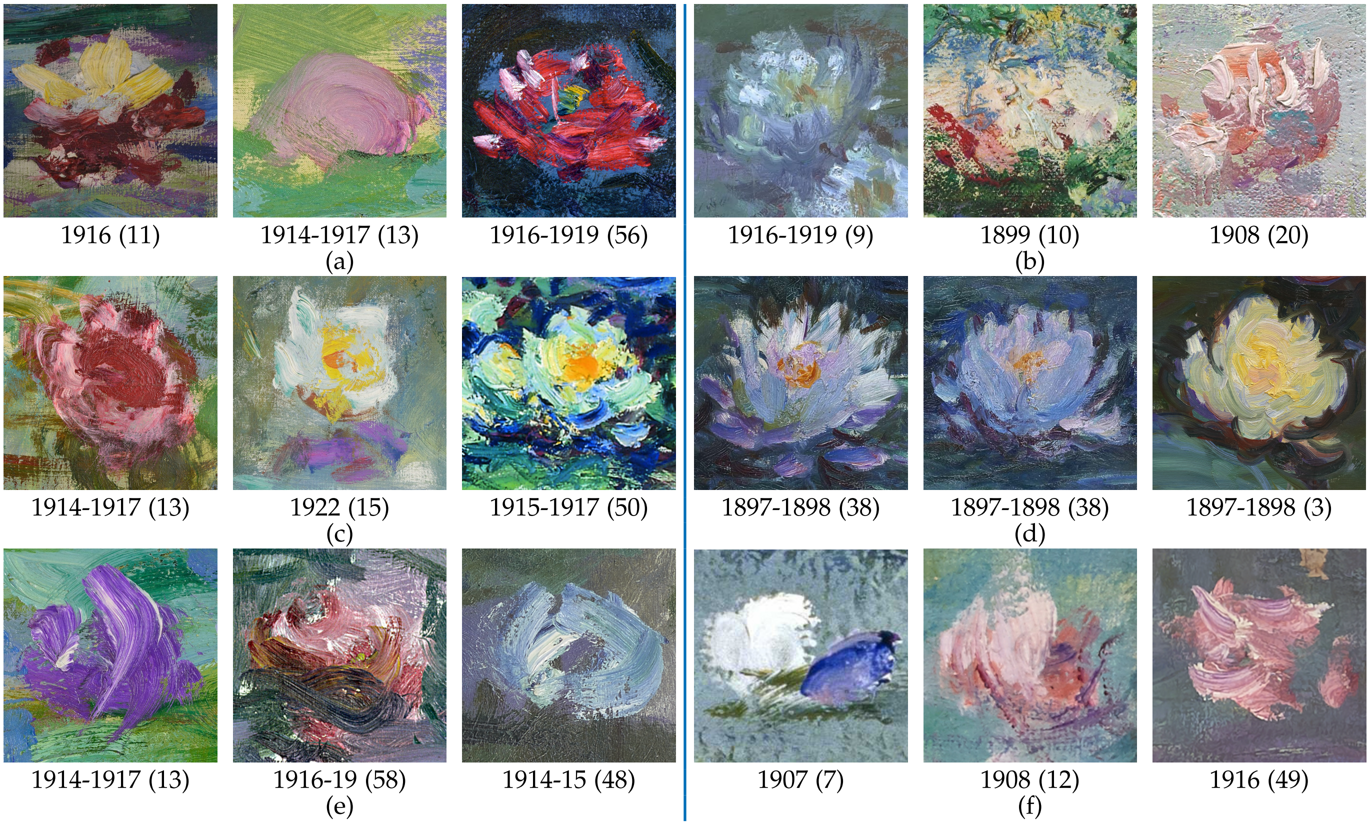

1916 (11) 1914-1917 (13) 1916-1919 (56)
(a)

1916-1919 (9) 1899 (10) 1908 (20)
(b)

1914-1917 (13) 1922 (15) 1915-1917 (50)
(c)

1897-1898 (38) 1897-1898 (38) 1897-1898 (3)
(d)

1914-1917 (13) 1916-19 (58) 1914-15 (48)
(e)

1907 (7) 1908 (12) 1916 (49)
(f)

Fig. 5. Example flower patches from different stylistic categories and time periods. The ID of the painting from which each patch is extracted is indicated in parentheses. (a) Abstract. (b) Non-abstract. (c) Quasi-abstract (late period). (d) Quasi-abstract (early period). (e) Sketchy abstract. (f) Sketchy non-abstract.

across all streamlines in an image serve as the input to G_c (CLAM). To better understand the extracted features, we first scale $\tilde{x}_1^*$ and $\tilde{x}_2^*$ to have unit standard deviation, and then apply an invertible linear transformation, denoted by $A = (a_{l,k})$, to the scaled two-dimensional data. Let the standard deviation of $\tilde{x}_j^*$ be $\tilde{\sigma}_j$, for $j = 1, 2$. We have

$$(x_1^*, x_2^*)^t = A \cdot (\tilde{x}_1^*/\tilde{\sigma}_1, \tilde{x}_2^*/\tilde{\sigma}_2)^t \ ,$$

where each row of A corresponds to one projection direction. Both projection directions are normalized to unit length but are not constrained to be orthogonal.

Let $(\bar{x}_1^*, \bar{x}_2^*)^t$ be the average of $(x_1^*, x_2^*)^t$ over all streamlines within a patch. The matrix A is optimized such that patch-wise feature vectors $(\bar{x}_1^*, \bar{x}_2^*)^t$ from the abstract class lie in the first quadrant, while those from the non-abstract class are distributed in the other three quadrants. Additionally, a regularization penalty is included to encourage orthogonal projection directions in A. In summary, the two projection directions applied to the original unscaled vector $(\tilde{x}_1^*, \tilde{x}_2^*)^t$ are $(a_{1,1}/\tilde{\sigma}_1, a_{1,2}/\tilde{\sigma}_2) = (-0.098, 0.779)$ and $(a_{2,1}/\tilde{\sigma}_1, a_{2,2}/\tilde{\sigma}_2) = (1.042, 0.234)$.

Fig. 6(a) displays the feature vectors $(\bar{x}_1^*, \bar{x}_2^*)^t$ for all patches. Patches from different paintings are shown in different colors; however, due to the large number of paintings and the limited distinctiveness of colors, twenty colors are cycled. Paintings from the early period are marked by a '+', while those from the late period are marked by an 'x'. Patches identified as abstract are highlighted with a circle around the symbol.

For the vast majority of patches, $\bar{x}_1^*$ effectively distinguishes abstract from non-abstract patches using a threshold at zero. Only a few early-period patches yield $\bar{x}_1^* > 0$. If we predict $\hat{Z} = 1$ when $\bar{x}_1^* \geq 0$, the error rate is as low as 2.89%. The second feature, $\bar{x}_2^*$, mainly serves to separate about a dozen non-abstract patches from abstract ones. However, this feature alone is weak at discriminating the two classes. If we predict $\hat{Z} = 1$ when $\bar{x}_2^* \geq 0$, the error rate rises to 82.31%. In contrast, if we predict $\hat{Z} = 1$ only when both $\bar{x}_1^* \geq 0$ and $\bar{x}_2^* \geq 0$, the error rate drops to 0.90%. In fact, 96.83% of patches with $Z = 0$ can be correctly classified based on $\bar{x}_1^* < 0$, and an additional 2.75% of $Z = 0$ patches can be correctly identified based on additionally $\bar{x}_2^* < 0$.

Fig. 6(b) shows a zoomed-in region of the scatter plot for $(\bar{x}_1^*, \bar{x}_2^*)^t$ among patches with $\bar{x}_1^* \geq 0$. The number next to each marker indicates the painting ID of the corresponding patch. There are five early-period patches with $\bar{x}_1^* > 0$. Of these, three have $\bar{x}_2^* < 0$, and one has $\bar{x}_2^*$ very close to zero (< 0.08). All four of these patches are close-up flowers from paintings with IDs 38 and 3. Three of these close-up flower patches are shown in Fig. 5(d). Among late-period patches with $\bar{x}_1^* > 0$ and $\bar{x}_2^* < 0$, there are twelve instances: seven come from painting 13, two from painting 56, and one each from paintings 15, 48, and 58. Two images—one from painting 56 and one from painting 58—lie near the boundary $\bar{x}_2^* = 0$, and DEGA classifies both as abstract.

Based on Fig. 6, we make the following observations:

1) Using the threshold $\bar{x}_1^* > 0$, 98.5% of early-period

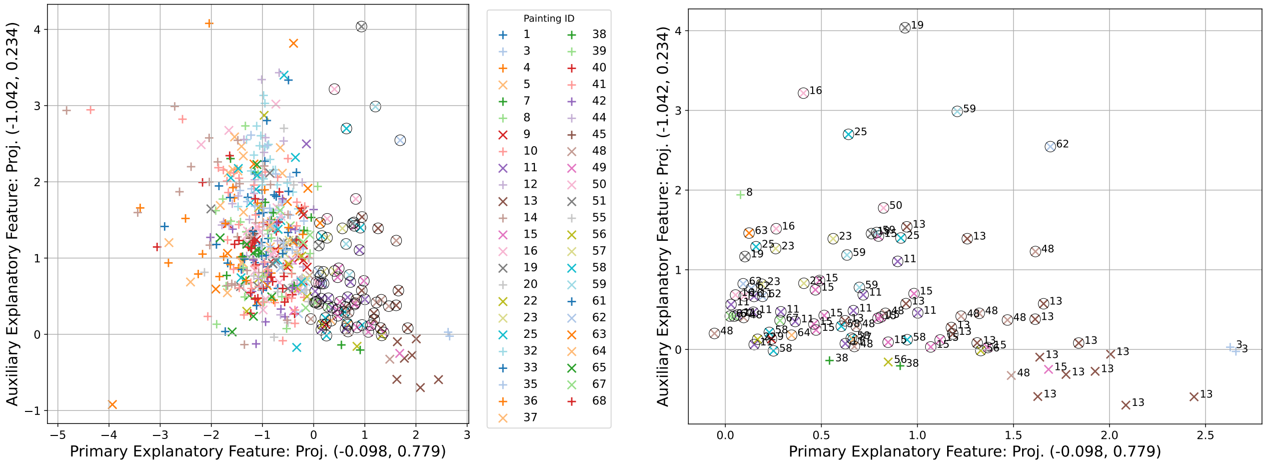

(a) (b)

Fig. 6. Scatterplot of average extracted feature vectors $(\bar{x}_1^*, \bar{x}_2^*)^t$ for 554 patches. Each point corresponds to a patch, with color indicating the painting of origin. Early-period patches are marked by '+' and late-period patches by 'x'. Patches identified as abstract are highlighted with a black circle. The distribution of patches across the four quadrants (I–IV), shown as $(Z = 0, Z = 1)$, is: (2, 78), (452, 1), (6, 0), and (13, 2), respectively. (a) Complete scatterplot. (b) Zoomed-in view of the region with $\bar{x}_1^* \geq 0$. The painting ID for each patch is shown beside its corresponding marker.

images are correctly identified as non-abstract, and 41% of late-period images are identified as abstract. This matches closely with the targeted ratio $\gamma = 37\%$.

2) Using the threshold $\bar{x}_2^* > 0$, the patches are divided into two highly imbalanced groups with 96.2% of the patches above the threshold. The value of $\bar{x}_2^*$ influences the prediction of Z for only a small subset of patches and is only weakly associated with abstractness. This feature was shaped during DEGA's training to help separate four early-period close-up flower patches from the abstract class, preventing their misclassification.

These observations indicate that $\bar{x}_1^*$ is the dominant feature in capturing the characteristics of the abstract style, while $\bar{x}_2^*$ plays a secondary role. Accordingly, we refer to $\bar{x}_1^*$ as the *primary explanatory feature*, and to $\bar{x}_2^*$ as the *auxiliary explanatory feature*.

Since the CLAM component of $\mathcal{M}_Z$ is applied to $(\bar{x}_1^*, \bar{x}_2^*)^t$ for patch-level classification, it can likewise be applied to $(x_1^*, x_2^*)^t$ of individual streamlines to classify them into $Z = 0$ or 1. While classifying individual streamlines is not necessary when the goal is to determine the class of a patch, such analysis proves useful for examining the primary and auxiliary explanatory features at the streamline level, or for interpreting them in terms of the streamlines' original geometric properties. This is especially important given the relatively small number of patches in the study, contrasted with over 70,000 streamlines across all patches.

To clarify how the primary and auxiliary explanatory features contribute to the classification of a patch or streamline as abstract or non-abstract, we organize these classes into a hierarchy. Specifically, we introduce the following subset definitions:

1) *Quasi-abstract*: An instance classified by $\mathcal{M}_Z$ as non-abstract ($Z = 0$), but exhibiting $x_1^* \geq 0$ and $x_2^* < 0$.
2) *Generalized abstract*: the union of the abstract and quasi-abstract classes (corresponding to $x_1^* \geq 0$).
3) *Strongly non-abstract*: non-abstract class excluding quasi-abstract instances.

The abstract, quasi-abstract, and non-abstract classes can be effectively distinguished by thresholding the values of x_1^* and x_2^*. The separation is not perfect due to the fact that the DEGA model $\mathcal{M}_Z$ uses an MLP classifier on the input $(x_1^*, x_2^*)^t$, which produces more flexible decision boundaries than those defined by the coordinate axes. However, this slight compromise in boundary simplicity yields a significant improvement in interpretability. Specifically, among the abstract class, 78 out of 81 patches lie in the first quadrant ($x_1^* > 0$, $x_2^* > 0$). All 13 patches in the quasi-abstract subclass are located in the fourth quadrant ($x_1^* > 0, x_2^* < 0$), which also contains two abstract patches whose x_2^* values are only slightly below zero. Within the non-abstract class, 458 out of 473 patches lie in the second and third quadrants, where $x_1^* < 0$.

4.4 Investigating Abstraction

Intriguingly, certain brushwork characteristics of close-up flowers from Monet's early period bear a striking resemblance to the so-called abstract style that emerges in his late period. This observation challenges conventional expectations of a definitive stylistic change in Monet's art, especially since early close-ups are rendered with meticulous detail. A closer look at the late-period abstract patches reveals that they are rarely close-up flowers. Instead, their brushstrokes flow with a fluid, expressive quality, contrasting with the spotty, somewhat disorderly strokes found in non-abstract patches. Some abstract patches carefully articulate floral anatomy, while others capture an entire bloom in a single, sweeping gesture. This complexity dispels any simplistic notion that Monet abandoned pictorial or gestural ideas that informed the creation of close-up floral studies earlier in his career.

This raises a compelling question for art historians: is the similarity between early close-up flower brushwork and late

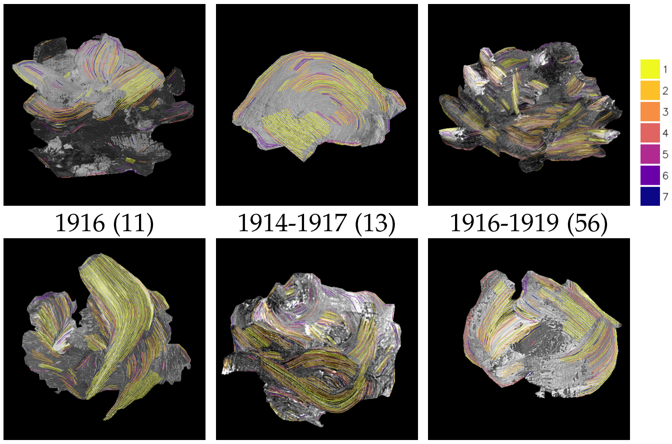

1916 (11) 1914-1917 (13) 1916-1919 (56)

1914-1917 (13) 1916-19 (58) 1914-1915 (48)

Abstract

1897-1898 (38) 1897-1898 (38) 1897-1898 (3)

Quasi-abstract

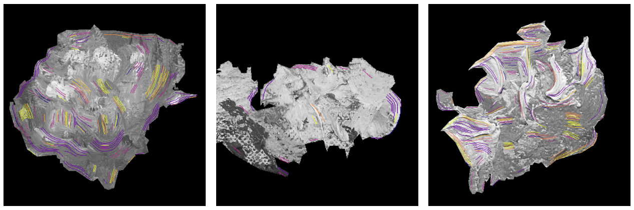

1916-1919 (9) 1899 (10) 1908 (20)

Non-abstract

Fig. 7. Streamlines overlaid on representative flower patches. The ID of the painting from which each patch is extracted is indicated in parentheses. The visualized streamlines belong to Assertive Regions (ARs) with IDs 1–7, as identified by the first decision tree used to classify patches based on the condition $x_1^* \geq 0$ versus $x_1^* < 0$, corresponding to generalized abstract and strongly non-abstract patches, respectively. Each streamline is color-coded according to its AR ID. The color palette strip on the right indicates the mapping between AR IDs and their assigned colors.

abstract style a curious coincidence, or is there a deeper conceptual and gestural thread linking these periods? Perhaps when Monet tackled expansive canvases in his late period, he instinctively employed the brushstroke strategies honed during his intimate early studies. Alternatively, Monet's brushwork may not be a conscious stylistic inheritance but rather a pragmatic response to artistic intention—when shifting from a focus on the delicate play of light on individual petals to an economy of means expressing floral form, his brushwork naturally aligned with a distinctive, gestural idiom. Our results offer a quantitative confirmation of a qualitative argument made by Denis Rouart about Monet's late work. Arguing against the idea that Monet became an abstract artist, Rouart suggests that Monet increasingly produced works that were partially figurative and partially "hermetic" (in the sense of a reduced relationship to the real world), thereby eluding any preconceived system or rigid set of art-historical categories [35].

Exploring this connection between Monet's early and later work from a quantitative perspective offers fertile ground for rethinking Monet's evolving technique—not as a linear progression, but as a dynamic interplay between observation, intention, and expressive freedom. The development of a machine learning framework to provide insight into fine-grained distinctions in Monet's brushwork offers, therefore, an important addition to debates about the artist's stylistic development that have unfolded over the course of a century.

Motivated by these intriguing questions, we investigate several approaches to elucidate the relationship between x_j^* ($j = 1, 2$) and the original streamline geometric features. While the derivation of x_j^* in the previous subsection has provided useful insights into their explanatory power, the features themselves remain to be interpreted in terms of the original geometry.

In Supplementary Materials, we provide plots comparing the kernel density functions (KDFs) of each original geometric feature across various data subsets—specifically, generalized abstract versus strongly non-abstract, and abstract versus quasi-abstract. We observe that the original features exhibit minimal differences in regions where the KDFs attain relatively high values, corresponding to the more frequently occurring feature values. This suggests that the relationship between x_j^* and the original geometric features is complex and not readily captured by simple distributional comparisons.

4.4.1 Linear Regression on Geometric Features

To interpret x_j^* ($j = 1, 2$) from a global perspective, we employ linear regression to examine their relationships with the original geometric features. Specifically, we treat x_j^* as the response variable and the original features as predictors, seeking a regression model that not only achieves reasonable predictive accuracy but also yields interpretable insights. To enhance interpretability, we exclude features that are highly correlated with each other. For example, since L_{norm} and $L_{\text{seg, norm}}$ are strongly correlated, we retain only L_{norm} due to its more straightforward interpretation. Likewise, between V_c and $\Delta\theta_{\text{ave}}$, which are also highly correlated, we choose to use V_c. We organize the 11 original features into five groups, each representing a distinct geometric aspect of the streamline: curvature, variation in curvature, length, wiggliness, and second-order curvature variation (see Supplementary Materials, available online for details). From each group, we select one representative feature. The selection is guided by two criteria: low mutual correlation among the chosen features and strong predictive performance for x_j^* using a linear model. The final selected features are: θ_{min} (minimum curvature), H_θ (entropy of curvature), L_{norm} (streamline length), V_c (average curvature change), $\sigma^2_{\Delta\theta}$ (variance of curvature change). The standard deviations of these features are 0.798, 0.16, 0.101, 0.722, and 0.249, respectively. In the regression models below, superscript "(s)" denotes that the feature has been scaled to unit variance.

This set of five features achieves the best predictive accuracy for x_2^* and performs nearly as well as the optimal

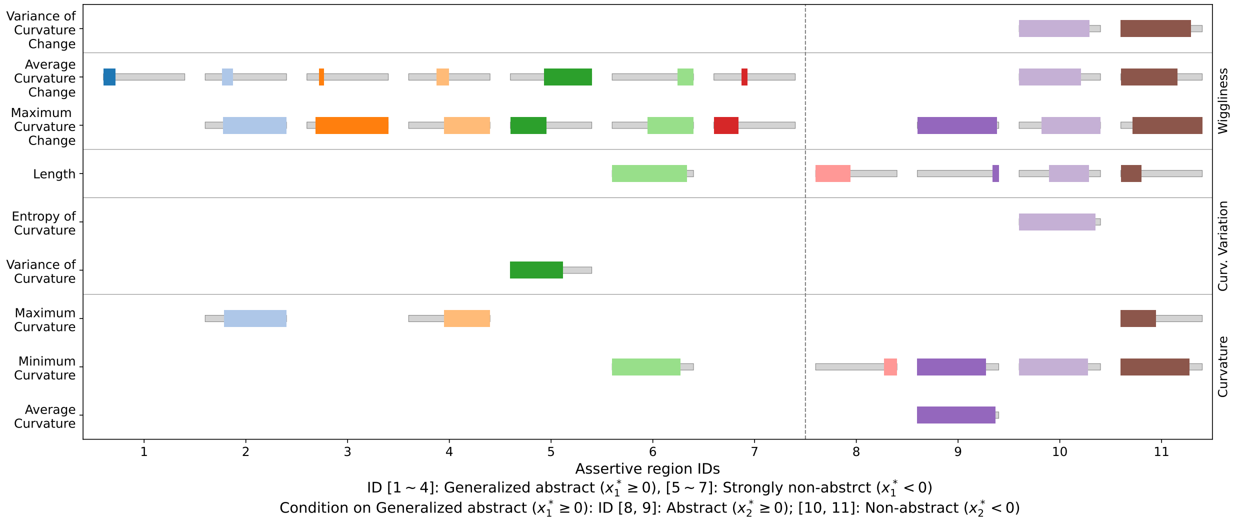

Fig. 8. Quantile Explanation Map (QEM) summarizing the defining conditions of ARs (assertive regions) with IDs 1–11. ARs 1–7 are derived from the first decision tree (for classifying broadly abstract versus strongly non-abstract), while ARs 8–11 are from the second tree (for classifying abstract versus quasi-abstract restricted to broadly abstract streamlines). The predicted majority class for each AR is indicated in the x-axis labels. Each column corresponds to an AR ID, and each row represents one of the nine geometric features of streamlines. A horizontal sliding bar is shown if the feature is involved in defining the AR. The thin gray bar spans the full percentile range (0–100) of that feature across all streamlines, while the colored bar indicates the specific percentile interval used to define the condition for that AR.

combination of predictor features for x_1^*. While the best-performing model for x_1^* uses σ_θ^2 (variance of curvature) instead of H_θ, the difference in the R^2 score is marginal, and H_θ is less correlated with the other selected features. The resulting regression functions are:

$$\begin{aligned}\hat{x}_1^* &= 2.859 + 0.23\theta_{\text{min}}^{(s)} + 0.31H_\theta^{(s)} + 0.33L_{\text{norm}}^{(s)} \\ &\quad -2.46V_c^{(s)} + 0.84\sigma_{\Delta\theta}^{2(s)} \\ \hat{x}_2^* &= -1.149 + 0.64\theta_{\text{min}}^{(s)} + 1.32H_\theta^{(s)} + 0.08L_{\text{norm}}^{(s)} \\ &\quad +0.88V_c^{(s)} + 0.28\sigma_{\Delta\theta}^{2(s)} \ .\end{aligned}$$

The corresponding R^2 values are 0.45 for $\hat{x}_1^*$ and 0.51 for $\hat{x}_2^*$, indicating moderate prediction power. These results suggest that x_1^* and x_2^* capture complex nonlinear relationships that are not easily approximated by linear combinations of the original features. Thus, while the regression models offer some interpretive value, they should be viewed as partial explanations rather than definitive mappings.

Since $x_1^* \geq 0$ indicates the generalized abstract style, the regression function for x_1^* suggests that such a style is associated with streamlines that are longer, exhibit greater curvature, show more variation in curvature, and display higher variability in wiggliness, while maintaining a lower average level of wiggliness—that is, they are overall smoother. In summary, streamlines characteristic of the abstract style tend to be longer and smoother, yet more diverse in their local geometric behavior, encompassing a broader range of curvature and wiggliness patterns.

Interestingly, these geometric characteristics are also present in quasi-abstract patches, including the close-up flower patches from the early period. A comparison between the regression models for x_1^* and x_2^* highlights a key difference between abstract and quasi-abstract classes: the role of V_c, which measures the local variability in curvature (i.e., how wiggly or smooth a streamline is). Streamlines from early-period close-up flower patches tend to be smoother—exhibiting lower V_c—than those from late-period abstract patches. This distinction in V_c suggests that smoothness is a critical factor differentiating quasi-abstract from abstract patches. In contrast, streamline length appears to play a more prominent role in distinguishing abstract from non-abstract patches than in distinguishing abstract from quasi-abstract ones, indicating that length alone is less decisive when the stylistic boundary is more nuanced.

4.4.2 *Interpretation based on Decision Trees*

We trained a decision tree to classify whether a streamline belongs to the generalized abstract class versus the strongly non-abstract class (that is, $x_1^* < 0$ versus $x_1^* \geq 0$) using the original geometric features of the streamlines. Nine of the eleven original features were retained; we excluded $L_{\text{norm,seg}}$ and $\Delta\theta_{\text{avg}}$ due to their near-perfect correlation with L_{norm} and V_c, respectively. The complexity parameter of the tree was selected using a validation subset consisting of a randomly chosen 20% of the data. After pruning, the resulting decision tree contains 40 leaf nodes. Similarly, we trained a second decision tree restricted to streamlines with $x_1^* \geq 0$, to classify whether $x_2^* \geq 0$ (that is, abstract versus quasi-abstract). Note that this decision is not intended to predict whether x_2^* is non-negative in a global sense, which stands in stark contrast to the linear regression function $\hat{x}_2^*$ described earlier. The pruned version of this tree yields 76 leaf nodes. The larger number of leaf nodes in the second tree suggests a more fragmented feature space to classify abstract from quasi-abstract, indicating greater complexity and reduced interpretability compared to the classification of generalized abstract versus strongly non-abstract. This supports the conclusion that the former task is more challenging than the latter. The two decision trees are shown in Supplementary Materials.

TABLE 2
Defining conditions of ARs (assertive regions) with IDs 1–11. ARs 1–7 correspond to the first decision tree (for classifying broadly abstract versus strongly non-abstract), and ARs 8–11 correspond to the second decision tree (for classifying abstract versus quasi-abstract restricted to broadly abstract streamlines). Each row lists the geometric features used to define an AR along with their value-based thresholds. The predicted majority class, the prediction accuracy, and the proportion of streamlines captured by each AR are also reported.

Type	AR ID	Conditions	Accuracy (%)	Proportion (%)
$x_1^* \geq 0$	1	$V_c \leq 0.170$	97.45	28.6
	2	$0.195 < V_c \leq 0.248$, $\Delta\theta_{\max} > 0.664$, $\theta_{\max} > 2.759$	95.33	12.8
	3	$0.170 < V_c \leq 0.195$, $\Delta\theta_{\max} > 0.486$	94.22	9.2
	4	$0.248 < V_c \leq 0.312$, $\Delta\theta_{\max} > 0.965$, $\theta_{\max} > 4.177$	92.92	9.2
$x_1^* < 0$	5	$V_c > 0.277$, $\Delta\theta_{\max} \leq 0.965$, $\sigma_\theta^2 \leq 2.347$	96.38	18.8
	6	$V_c > 0.512$, $\Delta\theta_{\max} > 0.965$, $\theta_{\min} \leq 0.624$, $L_{\text{norm}} \leq 0.235$	91.25	27.1
	7	$0.248 < V_c \leq 0.277$, $\Delta\theta_{\max} \leq 0.770$	90.84	5.2
Condition on $x_1^* \geq 0$				
$x_2^* \geq 0$	8	$\theta_{\min} > 0.557$, $L_{\text{norm}} \leq 0.064$	97.41	9.5
	9	$\theta_{\min} \leq 0.557$, $\theta_{\text{ave}} \leq 4.412$, $L_{\text{norm}} > 0.281$, $\Delta\theta_{\max} \leq 3.289$	97.22	6.1
$x_2^* < 0$	10	$\theta_{\min} \leq 0.557$, $0.055 < L_{\text{norm}} \leq 0.115$, $\sigma_{\Delta\theta}^2 \leq 0.162$, $\Delta\theta_{\max} > 0.633$, $V_c \leq 0.342$, $H_\theta \leq 0.089$	98.32	20.9
	11	$\theta_{\min} \leq 0.557$, $\theta_{\max} \leq 3.528$, $L_{\text{norm}} \leq 0.045$, $\sigma_{\Delta\theta}^2 \leq 0.162$, $\Delta\theta_{\max} > 0.455$, $V_c \leq 0.305$	96.71	7.7

For each tree, we identify ARs (assertive regions). Table 2 lists the defining conditions for each AR, along with its predicted class, its classification accuracy, and the proportion of data points it covers. The 11 identified ARs are indexed from 1 to 11. In general, ARs defined by fewer conditions are easier to interpret. The ARs distinguishing generalized abstract from strongly non-abstract tend to have simpler conditions compared to those distinguishing abstract from quasi-abstract. This again suggests that the quasi-abstract versus abstract distinction is more complex than the abstract versus non-abstract distinction.

Specifically, for the generalized abstract class, four ARs are identified, collectively covering 59.8% of the streamlines in this subset. For strongly non-abstract, three ARs cover 51.1% of the corresponding streamlines. In contrast, only two ARs are identified in each class of the quasi-abstract versus abstract split: for the abstract class, they cover 28.6% of the streamlines; for quasi-abstract class, they cover only 15.6%. This contrast reinforces the notion that explaining the quasi-abstract versus abstract distinction is more difficult than explaining the abstract versus non-abstract distinction.

In Fig. 7, streamlines are overlaid on grayscale flower patches. For clarity, not all detected streamlines in each patch are shown. We display only the streamlines that belong to ARs with IDs 1–7, which are derived from the first decision tree used to classify $x_1^* \geq 0$ (generalized abstract) versus $x_1^* < 0$ (strongly non-abstract). Streamlines that belong to ARs with IDs 8-11 are shown in another figure in Supplementary Materials. The streamlines are color-coded according to their corresponding AR IDs, with the color palette strip indicating the color assigned to each AR.

To better visualize the conditions of the ARs listed in Table 2, we created a *Quantile Explanation Map (QEM)* in Fig. 8. Each label on the x-axis corresponds to an AR ID, while the y-axis lists the nine geometric features of streamlines. For each feature involved in defining an AR, a sliding bar is shown. The thin gray bar indicates the full percentile range from 0 to 100, and the wider colored bar highlights the specific percentile range used to define the AR. For example, AR 1 is defined by the condition $V_c \leq 0.170$, where the threshold 0.170 corresponds to the 14.71st percentile of V_c. Since there is no lower bound specified, the colored bar spans from the 0th to the 14.71st percentile on percentile bar for feature V_c.

The QEM reveals which features are most frequently used to define ARs and highlights the geometric characteristics that contribute to classification. Two features—V_c and $\Delta\theta_{\max}$—appear most frequently and both reflect the "wiggliness" of streamlines. However, they do not always imply the same geometric tendency. For instance, in AR 5, which predicts $x_1^* < 0$, streamlines are highly wiggly on average according to V_c but relatively smooth where the curvature changes the fastest, as indicated by a low value of $\Delta\theta_{\max}$. This contrast is not contradictory, but reflects the subtle complexity of streamline shapes: streamlines may exhibit moderate to high average local curvature changes while having a relatively low maximum local curvature change. Another notable pattern involves the normalized length L_{norm}. This feature is used in all four ARs that distinguish $x_2^* < 0$ from $x_2^* \geq 0$, but it appears in only one AR predicting $x_1^* < 0$, and even there, it merely excludes the upper tail of the distribution. This suggests that streamline length is more informative for distinguishing quasi-abstract from abstract—given that the streamline is already known to be generalized abstract—than for distinguishing abstract from non-abstract.

It is informative to examine the conditions associated with the ARs. For example, AR 1 accounts for 28.6% of streamlines in the generalized abstract class and is defined by a single condition on V_c, requiring it to be below the

14.71st percentile. This implies that a streamline is highly likely to belong to the generalized abstract class as opposed to the strongly non-abstract class if it is sufficiently smooth according to the V_c measure. In AR 8, streamlines are predicted to fall into the abstract class as opposed to the quasi-abstract class. This rule specifies that the normalized length L_{norm} must be below the 42.79th percentile, while the minimum curvature θ_{min} must exceed the 84.28th percentile. Thus, streamlines of short to moderate length combined with high minimum curvature tend to distinguish abstract from quasi-abstract instances.

5 ART-HISTORICAL INSIGHTS

This research used machine learning to offer new insight into Monet's stylistic evolution in the rendering of the water lily motif and, by extension, into the artist's development of a so-called abstract style of mark-making. Our results challenge dominant art-historical narratives that posit a definitive turn to abstraction in Monet's late work. By isolating and mapping detailed directional flows of brushwork across a wide chronological sample of Monet's *Water Lilies*, our framework identified surprising gestural similarities between the artist's early and late approaches to this subject. This result opens new perspectives on Monet's creative practice by suggesting that the artist had a distinctive and, to a significant extent, consistent practice in rendering the water lily motif regardless of how realistic or abstract that motif looks to the viewer of the final work of art.

Our results also prompt a reconsideration of the relationship between Monet's eye problems and his late painting style. While scholars have debated changes in Monet's palette and style as his eyesight deteriorated (sometimes positing this as the reason for a turn to abstraction) [23], [36], the presence of brushwork consistencies across early and later works suggests that gestural memory might have played a large part in Monet's late painting regardless of the artist's visual perception of the world around him.

Our study reveals the need to approach Monet's *Water Lilies* holistically and to understand the central motif as a unifying factor both thematically *and* gesturally. Tracking the directional flow of brushmarks allows for a better understanding of a consistent pictorial logic underpinning this important part of Monet's output and shows how the water lily motif was capable of serving as a visual anchor regardless of the more or less naturalistic rendering of the surroundings. The presence of recurring brushmark patterns within the *Water Lilies* also demonstrates the artist's consistent approach to this motif regardless of the scale of the paintings or the size of brush employed. Taken together, these outcomes offer a new interpretation of Monet's stylistic development and an alternative narrative of the artist's association with categories of abstract art.

Finally, the results of our study suggest a new way of conceptualizing the idea of 'late style' itself. Edward Said famously described late style as evidence of an artist's encounter with 'intransigeance, difficulty, and unresolved contradiction' rather than the attainment of harmony and resolution [37]. The multiple temporal relations that Said identified in late style operate, therefore, as a counterweight to critical narratives of progress that posit an artist's achievement of a culminating creative idiom. In support of Said's thesis, our machine learning framework encourages an understanding of Monet's 'late style' as plural and capable of opening routes into the artist's own history of mark-making.

6 CONCLUSIONS

We introduced a novel machine learning framework, DEGA, for identifying a distinct artistic style within paintings from a specific historical period. This task departs from conventional classification problems in that the target style represents a latent subclass embedded within a subset of the data. Leveraging a custom streamline-based image representation and a new deep neural network architecture, C2A, our analysis uncovered an emergent abstract style in the later works of Monet's *Water Lilies* while also demonstrating important consistencies with earlier brushwork. We conducted an in-depth examination of the relationship between this emerging abstract class and the underlying geometric features of the streamlines. By employing multiple feature interpretation techniques, we identified quantifiable visual conditions under which one can reliably infer that an image patch belongs to a distinct artistic style.

These findings challenge long-standing art-historical narratives about Monet's path to abstraction and offer a more nuanced account of his stylistic development. Because there is no unitary concept of 'abstraction' and distinctions between abstract and non-abstract styles are heavily context-dependent, our analysis should be understood in light of this interpretive flexibility. This entails recognition that both algorithmic and human factors will inevitably combine to shape the results of the analysis. Even so, this convergence of machine learning and art history generates a new interpretive lens through which to reassess stylistic categories more generally and to better investigate continuities and changes in an individual artist's creative output. The framework could usefully be expanded to the study of other artist's works and underscores how innovative interdisciplinary approaches can answer important questions in the humanities while opening new computational challenges.

REFERENCES

[1] J. Royer, J. Haut, and P. Amalric, "L'opération de la cataracte de claude monet: Correspondance inédite du peintre et de g. clemenceau au docteur coutela," in *Meeting of 17 March of the Société française d'histoire de la médecine*, 1984, pp. 109–127.

[2] D. G. Stork, "Computer vision, ML, and AI in the study of fine art," *Communications of the ACM*, vol. 67, no. 5, pp. 68–75, 2024.

[3] J. Z. Wang, B. Kandemir, and J. Li, "Computerized analysis of paintings," in *The Routledge Companion to Digital Humanities and Art History*. Routledge, 2020, pp. 299–312.

[4] Z. Sabetsarvestani, B. Sober, C. Higgitt, I. Daubechies, and M. R. Rodrigues, "Artificial intelligence for art investigation: Meeting the challenge of separating x-ray images of the Ghent Altarpiece," *Science Advances*, vol. 5, no. 8, p. eaaw7416, 2019.

[5] L. Shamir, "What makes a Pollock Pollock: a machine vision approach," *International Journal of Arts and Technology*, vol. 8, no. 1, pp. 1–10, 2015.

[6] ——, "Computer analysis reveals similarities between the artistic styles of Van Gogh and Pollock," *Leonardo*, vol. 45, no. 2, pp. 149–154, 2012.

[7] A. Pizurica, L. Platisa, T. Ruzic, B. Cornelis, A. Dooms, M. Martens, H. Dubois, B. Devolder, M. De Mey, and I. Daubechies, "Digital image processing of the Ghent Altarpiece: Supporting the painting's study and conservation treatment," *IEEE Signal Processing Magazine*, vol. 32, no. 4, pp. 112–122, 2015.

[8] S. Lyu, D. Rockmore, and H. Farid, "A digital technique for art authentication," *Proceedings of the National Academy of Sciences*, vol. 101, no. 49, pp. 17 006–17 010, 2004.

[9] J. Li, L. Yao, E. Hendriks, and J. Z. Wang, "Rhythmic brushstrokes distinguish Van Gogh from his contemporaries: Findings via automated brushstroke extraction," *IEEE Transactions on Pattern Analysis and Machine Intelligence*, vol. 34, no. 6, pp. 1159–1176, 2012.

[10] Z. Zhang, E. C. Mansfield, J. Li, J. Russell, G. S. Young, C. Adams, K. A. Bowley, and J. Z. Wang, "A machine learning paradigm for studying pictorial realism: How accurate are Constable's clouds?" *IEEE Transactions on Pattern Analysis and Machine Intelligence*, vol. 46, no. 1, pp. 33–42, 2023.

[11] I. Santos, L. Castro, N. Rodriguez-Fernandez, A. Torrente-Patino, and A. Carballal, "Artificial neural networks and deep learning in the visual arts: A review," *Neural Computing and Applications*, vol. 33, pp. 121–157, 2021.

[12] Y. Bar, N. Levy, and L. Wolf, "Classification of artistic styles using binarized features derived from a deep neural network," in *Proceeding of the European Conference on Computer Vision Workshops, Part I*. Springer, 2015, pp. 71–84.

[13] S. Agarwal, H. Karnick, N. Pant, and U. Patel, "Genre and style based painting classification," in *Proceedings of the IEEE Winter Conference on Applications of Computer Vision*. IEEE, 2015, pp. 588–594.

[14] Y. Jing, Y. Yang, Z. Feng, J. Ye, Y. Yu, and M. Song, "Neural style transfer: A review," *IEEE Transactions on Visualization and Computer Graphics*, vol. 26, no. 11, pp. 3365–3385, 2019.

[15] J. Sheng, C. Song, J. Wang, and Y. Han, "Convolutional neural network style transfer towards Chinese paintings," *IEEE Access*, vol. 7, pp. 163 719–163 728, 2019.

[16] A. Semmo, T. Isenberg, and J. Döllner, "Neural style transfer: A paradigm shift for image-based artistic rendering?" in *Proceedings of the Symposium on Non-photorealistic Animation and Rendering*, 2017, pp. 1–13.

[17] E. Gultepe, T. E. Conturo, and M. Makrehchi, "Predicting and grouping digitized paintings by style using unsupervised feature learning," *Journal of Cultural Heritage*, vol. 31, pp. 13–23, 2018.

[18] E. E. Robles, Y. Jin, P. Smyth, R. H. Scheuermann, J. D. Bui, H.-Y. Wang, J. Oak, and Y. Qian, "A cell-level discriminative neural network model for diagnosis of blood cancers," *Bioinformatics*, vol. 39, no. 10, p. btad585, 2023.

[19] E. Arvaniti and M. Claassen, "Sensitive detection of rare disease-associated cell subsets via representation learning," *Nature Communications*, vol. 8, no. 1, p. 14825, 2017.

[20] P. Mille, "Écrits sur l'eau," *Le Temps*, p. 3, May 13, 1909.

[21] L. Vauxcelles, "Claude monet," *L'Amour de l'art*, pp. 230–236, Nov. 1922.

[22] L. Gillet, *Trois Variations sur Claude Monet*. Paris, France: Librairie Plon, 1927.

[23] P. Jamot, *Claude Monet: Exposition Rétrospective*. Musée de l'Orangerie, Paris, 1931.

[24] J. Lewinson, *Turner, Monet, Twombly: Later Paintings*. Moderna Museet, 2011.

[25] C. Debray, *L'Abstraction Américaine et le Dernier Monet*. Musée d'Orsay, 2018.

[26] S. Pagé, *Monet Mitchell*. Fondation Louis Vuitton/Hazan, 2022.

[27] C. Greenberg, *Art and Culture: Critical Essays*. Beacon Press, 1969.

[28] A. Kirillov, E. Mintun, N. Ravi, H. Mao, C. Rolland, L. Gustafson, T. Xiao, S. Whitehead, A. C. Berg, W.-Y. Lo *et al.*, "Segment anything," in *Proceedings of the IEEE/CVF International Conference on Computer Vision*, 2023, pp. 4015–4026.

[29] Z. Zhang, J. Li, D. G. Stork, E. Mansfield, J. Russell, C. Adams, and J. Z. Wang, "Reducing bias in ai-based analysis of visual artworks," *IEEE BITS the Information Theory Magazine*, vol. 2, no. 1, pp. 36–48, 2022.

[30] V. B. S. Prasath, R. Pelapur, G. Seetharaman, and K. Palaniappan, "Multiscale structure tensor for improved feature extraction and image regularization," *IEEE Transactions on Image Processing*, vol. 28, no. 12, pp. 6198–6210, 2019.

[31] P. Alarco, T. Dufrêne, and M. Draguet, *Monet et l'Abstraction: exposition, Paris, Musée Marmotan, 16 Juin–26 septembre 2010*. Hazan, 2010.

[32] B. Fer, *On Abstract Art*. Yale University Press, 2000.

[33] Y. Gorishniy, I. Rubachev, V. Khrulkov, and A. Babenko, "Revisiting deep learning models for tabular data," *Advances in neural information processing systems*, vol. 34, pp. 18 932–18 943, 2021.

[34] J. House, *Monet: Nature into Art*. Yale University Press, 1986).

[35] J. D. Rey and D. Rouart, *Monet: Les Nymphéas. L'Intégralité*. Flammarion, 2016, ch. Apparences et reflets.

[36] A. Gruener, "The effects of cataracts and cataract surgery on Claude Monet," *British Journal of General Practice*, vol. 65, no. 634, pp. 254–255, 2015.

[37] E. Said, *On Late Style*. Bloomsbury, 2006.

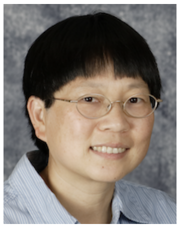

Jia Li (Fellow, IEEE) is a Professor of Statistics and (by courtesy) Computer Science and Engineering at The Pennsylvania State University. Her research interests include machine learning, artificial intelligence, probabilistic graph models, and image analysis. She worked as a Program Director at the NSF from 2011 to 2013, a Visiting Scientist at Google Labs in Pittsburgh from 2007 to 2008, a researcher at the Xerox Palo Alto Research Center from 1999 to 2000, and a Research Associate in the Computer Science Department at Stanford University in 1999. She received the MS degree in Electrical Engineering (1995), the MS degree in Statistics (1998), and the PhD degree in Electrical Engineering (1999), from Stanford University. She was Editor-in-Chief for Statistical Analysis and Data Mining: The ASA Data Science Journal from 2018 to 2020. She is a Fellow of the Institute of Electrical and Electronics Engineers and a Fellow of the American Statistical Association.

Chaewan Chun is a doctoral candidate in the College of Information Sciences and Technology at The Pennsylvania State University. She received a bachelor's degree in computer science, graduating *magna cum laude* from the Schreyer Honors College, along with a bachelor's degree in mathematics from Penn State in 2022.

Kathryn Brown is a Reader in art histories, markets and digital heritage at Loughborough University, United Kingdom. Her publications span nineteenth- and twentieth-century French art, digital art history, contemporary art, and the art market. She researches at the intersection of AI and art history and is the principal investigator on the AHRC-funded project to model a Museum of AI Cultures. Her books include *Women Readers in French Painting 1870–1890* (2012), *Matisse's Poets: Critical Performance in the Artist's Book* (2017), *Henri Matisse* (2021), *Dialogues with Degas* (2023), and *Art Auctions: Spectacle and Value in the 21st Century* (2024). Her latest edited collection, *Artificial Intelligence and Art History: Looking at Images in an Algorithmic Culture* will be published in 2026 in the *Proceedings of the British Academy*. Brown has held visiting fellowships at the Center for Advanced Studies in the Visual Arts (Washington DC), the Beinecke Rare Book and Manuscript Library (Yale University) and the Getty Research Institute (Los Angeles). She is the series editor of *Contextualizing Art Markets* for Bloomsbury Academic.

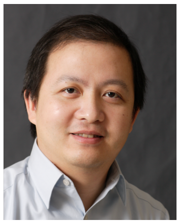

James Z. Wang (Senior Member, IEEE) is a Distinguished Professor in the Department of Informatics and Intelligent Systems in the College of Information Sciences and Technology at The Pennsylvania State University. He received the bachelor's degree in mathematics, *summa cum laude*, from the University of Minnesota (1994), and the MS degree in mathematics (1997), the MS degree in computer science (1997), and the PhD degree in medical information sciences (2000), all from Stanford University. His research interests include image analysis, affective computing, image modeling, image retrieval, and their applications. He was a visiting professor at the Robotics Institute at Carnegie Mellon University (2007-2008), a lead special section guest editor of the IEEE Transactions on Pattern Analysis and Machine Intelligence (2008), a program manager at the Office of the Director of the NSF (2011-2012), and a special issue guest editor of the IEEE BITS—The Information Theory Magazine (2022). He was a recipient of an NSF Career Award (2004) and Amazon Research Awards (2018-2022).

Supplementary Materials for "Computational Investigation of Abstraction in Claude Monet's *Water Lilies* through Brushstroke Analysis"

Jia Li, *Fellow, IEEE,* Chaewan Chun, Kathryn Brown, and James Z. Wang, *Senior Member, IEEE*

1 PAINTING INFORMATION

Table 1 presents information on all paintings included in our study. Fig. 1– 4 show thumbnails of the paintings.

2 STREAMLINE GEOMETRIC FEATURES

The 11 features computed for each streamline are defined below. Recall that a streamline is represented by an ordered sequence of pixels, $(\zeta_i, \eta_i) \mid i = 1, \ldots, n$. At each pixel $(\zeta_i, \eta_i), i = \delta{+}1, \delta{+}2, ..., n{-}\delta$, where $\delta = 3$, we compute θ_i, the turning angle of the streamline, as well as $\Delta\theta_i$, the absolute change in turning angles between consecutive pixels.

1) Average Turning Angle/Average Curvature:

$$\theta_{\text{ave}} = \frac{1}{n - 2\delta} \sum_{i=\delta+1}^{n-\delta} \theta_i \ .$$

2) Minimum Turning Angle/Minimum Curvature:

$$\theta_{\min} = \min_i(\theta_i) \ .$$

3) Maximum Turning Angle/Maximum Curvature:

$$\theta_{\max} = \max_i(\theta_i) \ ,$$

which captures the sharpest turn along the streamline.

4) Variance of Turning Angles/Variance of Curvature:

$$\sigma_\theta^2 = \frac{1}{n - 2\delta - 1} \sum_{i=\delta+1}^{n-\delta} (\theta_i - \theta_{\text{ave}})^2 \ .$$

σ_θ^2 reflects the variation in curvature along the streamline. A streamline exhibiting a broad range of curvature values tends to produce a large σ_θ^2.

5) Entropy of Turning Angles/Entropy of Curvature: We divide the full angle range $[0, 180°]$ into 18 equal bins, each spanning $10°$ and starting at $0°$. Let n_k denote the number of turning angles (the θ_i's) that fall into the kth bin. The probability associated with the kth bin is defined as $q_k = n_k / \sum_{j=1}^{18} n_j$. The Shannon entropy is then computed as $H_\theta = -\sum_{k=1}^{18} q_k \log_2(q_k)$. Following standard convention, we set $q_k \log_2(q_k) = 0$ whenever $q_k = 0$. This entropy quantifies the randomness in the distribution of turning angles along the streamline. It tends to be high when curvature values are diverse and unpredictably distributed.

6) Normalized Streamline Length:

$$L_{\text{norm}} = \frac{\sum_{i=1}^{n-1} \|(\zeta_{i+1} - \zeta_i, \eta_{i+1} - \eta_i)^t\|}{\sqrt{n_w \cdot n_h}} \ ,$$

where n_w and n_h are the width and height of the image respectively.

7) Length of the Longest Smooth Segment: A smooth segment is defined as a consecutive sequence of pixels along a streamline where the corresponding $\Delta\theta_i \leq 10°$. For each streamline, we identify the longest such segment and denote its length by L_{seg}. This length is then normalized by the image size, and the resulting value is used as a feature:

$$L_{\text{seg,norm}} = \frac{L_{\text{seg}}}{\sqrt{n_w \cdot n_h}} \ .$$

8) Maximum Turning Angle Change/Maximum Curvature Change:

$$\Delta\theta_{\max} = \max_i(\Delta\theta_i) \ .$$

9) Average Turning Angle Change:

$$\Delta\theta_{\text{avg}} = \frac{1}{n - 2\delta - 1} \sum_{i=\delta+2}^{n-\delta} \Delta\theta_i \ .$$

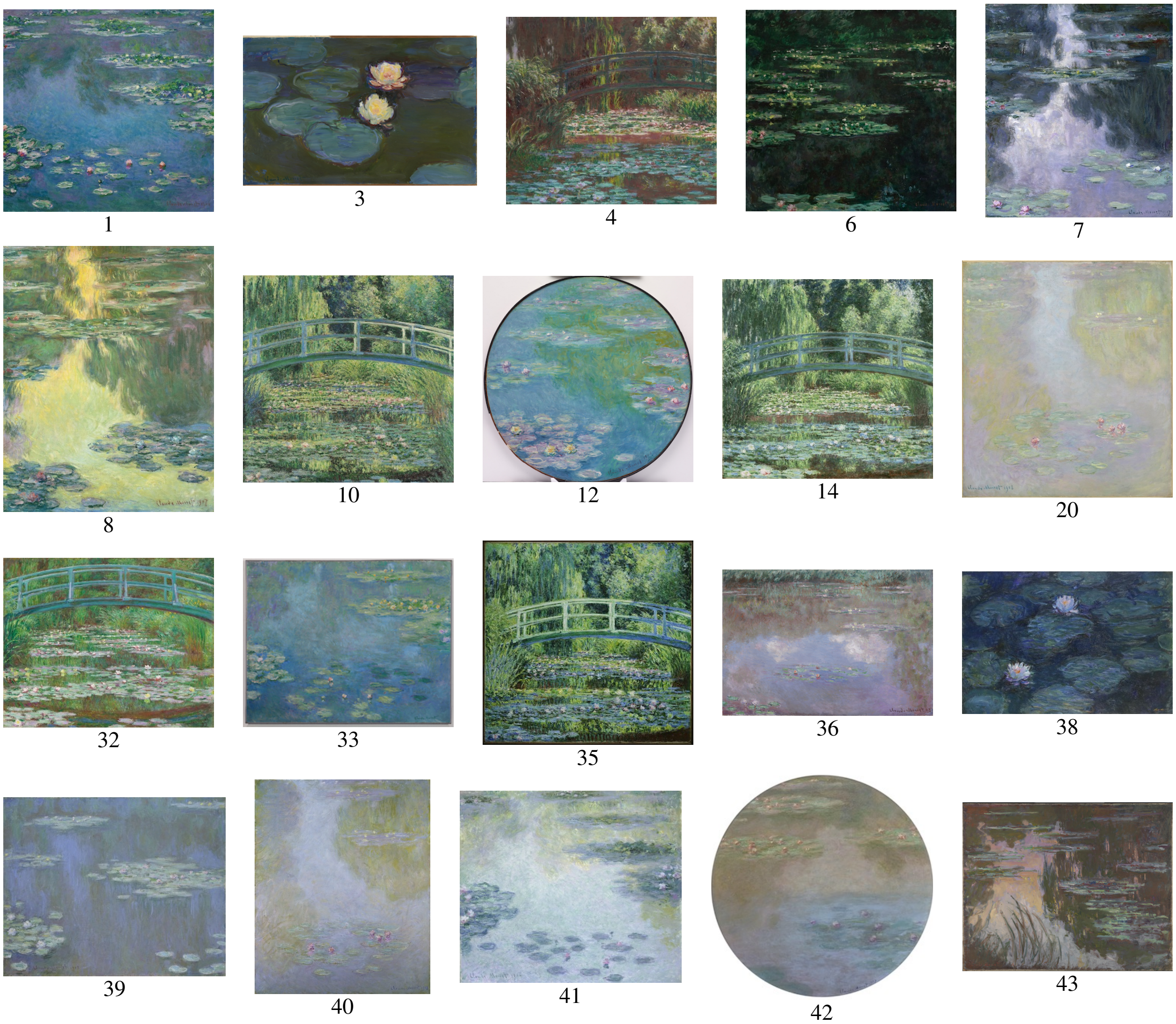

Fig. 1: Thumbnails of Monet’s early-period paintings, part 1 (first 20 images, IDs 1–43), ordered by catalogue ID.

$\Delta\theta_{\text{avg}}$ measures how ”wiggly” the curve is on average.

10) Average Curvature Change:

$$V_c = \frac{\sum_{i=\delta+2}^{n-\delta} \Delta\theta_i}{\sum_{i=\delta+2}^{n-\delta} \|(\zeta_i - \zeta_{i-1}, \eta_i - \eta_{i-1})^t\|} \,.$$

V_c quantifies the average ‘wiggliness’ of the curve, closely resembling $\Delta\theta_{\text{ave}}$; the primary distinction lies in their normalization factors.

11) Variance of Turning Angle Change/Variance of Curvature Change:

$$\sigma^2_{\Delta\theta} = \frac{1}{n - 2\delta - 2} \sum_{i=\delta+2}^{n-\delta} (\Delta\theta_i - \Delta\theta_{\text{ave}})^2 \,.$$

$\sigma^2_{\Delta\theta}$ measures the variation in local curvature changes along the streamline. For example, a streamline that alternates between smooth and wiggly segments tends to yield a high value of $\sigma^2_{\Delta\theta}$.

3 STREAMLINES FOR EXAMPLE IMAGES

In Fig. 5, only streamlines that belong to ARs with IDs 8–11, obtained from the second decision tree used to classify $x_2^* \geq 0$ (abstract) versus $x_2^* < 0$ (quasi-abstract), are shown. The streamlines are color-coded according to their corresponding AR IDs, with the color palette strip indicating the color assigned to each AR.

4 COMPARISON OF INDIVIDUAL GEOMETRIC FEATURES IN DIFFERENT GROUPS

In Fig. 6, we compare the kernel density functions (KDFs) of each original geometric feature across different subsets of

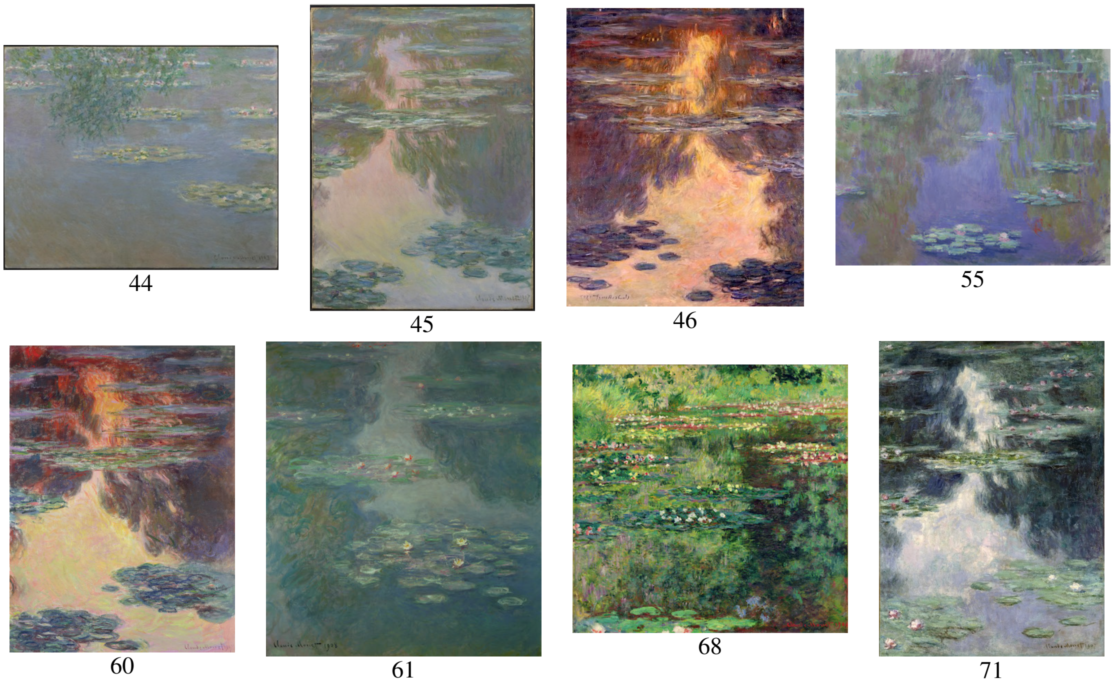

Fig. 2: Thumbnails of Monet's early-period paintings, part 2 (remaining images, IDs 44–71).

the data. In Fig.6(a), KDFs are shown for streamlines with $x_1^* < 0$ (strongly non-abstract) versus $x_1^* \geq 0$ (generalized abstract). In Fig. 6(b), we further subdivide the streamlines with $x_1^* \geq 0$ into two groups based on $x_2^* < 0$ (quasi-abstract) and $x_2^* \geq 0$ (abstract). Since the differences between KDFs are often subtle in the linear scale, we plot the distributions on a logarithmic scale for better visibility.

For the comparison between generalized abstract and strongly non-abstract (Fig. 6(a)), we observe that the original features show little difference where the KDFs are relatively high—that is, among the more common values. The distinctions emerge primarily in the distribution tails. For example, in the case of minimum curvature (that is, θ_{min}), streamlines with $x_1^* \geq 0$ exhibit notably higher extreme values. This suggests that when a streamline has extremely high minimum curvature, it is almost certainly associated with $x_1^* \geq 0$. However, such extreme cases are exceedingly rare, and thus account for a negligible fraction of the data. The observed divergence at the tails may also be partially attributed to the unreliability of density estimation in regions with very few samples.

In contrast, Fig. 6(b) reveals more substantial differences in KDFs between abstract and quasi-abstract, among generalized abstract streamlines. Across all geometric features, the group with $x_2^* \geq 0$ consistently exhibits a broader range, extending to much higher values. This may be partially explained by the fact that a significantly larger proportion of streamlines fall into the $x_2^* \geq 0$ group.

5 DECISION TREES

The first decision tree, shown in Fig. 7, classifies generalized abstract ($x_1^* \geq 0$) versus strongly non-abstract ($x_1^* < 0$) cases. The second tree, shown in Fig. 8, further classifies the generalized abstract class ($x_1^* \geq 0$) into abstract ($x_2^* \geq 0$) and quasi-abstract ($x_2^* < 0$) cases.

Fig. 3: Thumbnails of Monet’s late-period paintings, part 1 (first 20 images, IDs 5–48), ordered by catalogue ID.

Fig. 4: Thumbnails of Monet’s late-period paintings, part 2 (remaining images, IDs 49–77).

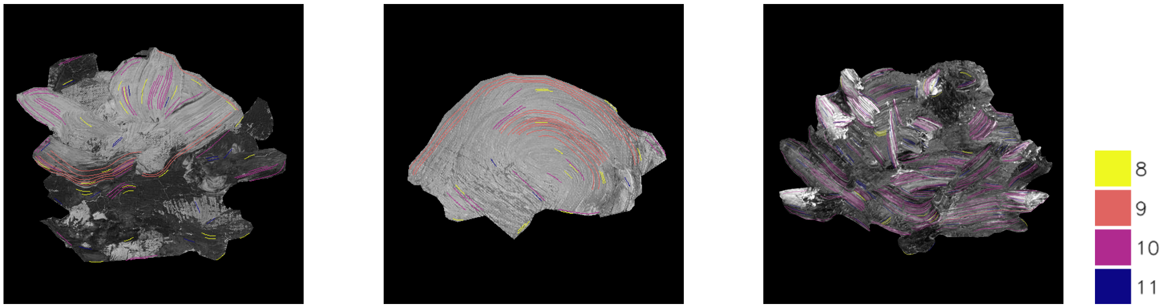

1916 (11) 1914-1917 (13) 1916-1919 (56)

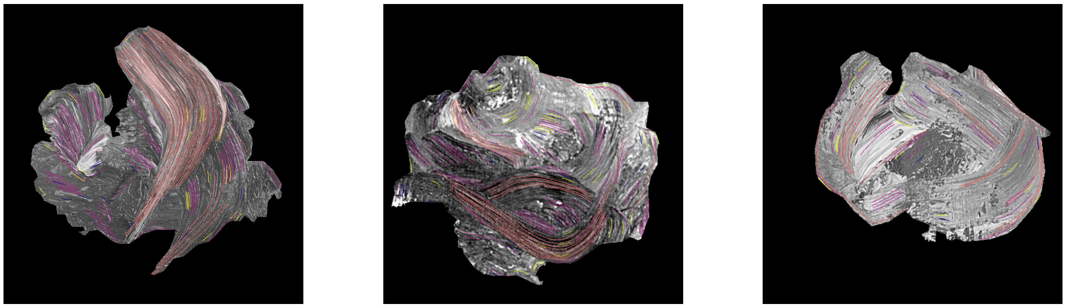

1914-1917 (13) 1916-19 (58) 1914-1915 (48)

Abstract

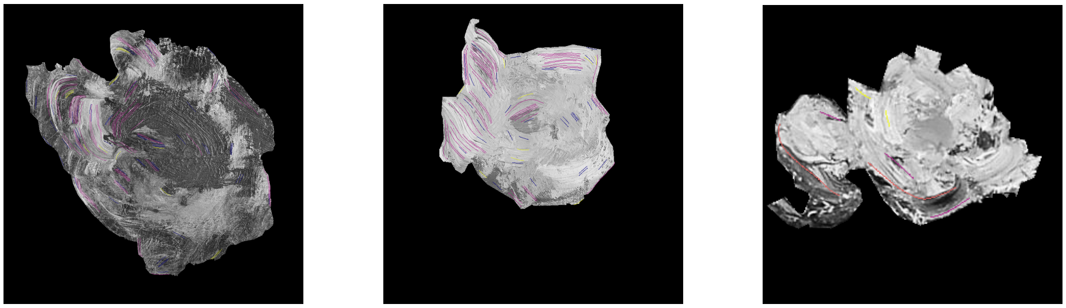

1914-1917 (13) 1922 (15) 1915-1917 (50)

Quasi-abstract (Late period)

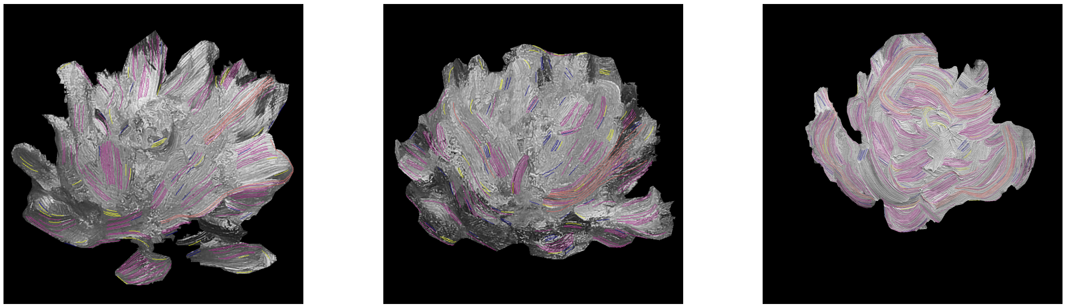

1897-1898 (38) 1897-1898 (38) 1897-1898 (3)

Quasi-abstract (Early period, close-up)

Fig. 5: Streamlines overlaid on example flower patches. The ID of the painting from which each patch is extracted is indicated in parentheses. The displayed streamlines belong to Assertive Regions (ARs) with IDs 8–11, identified by the second decision tree used to classify $x_2^* \geq 0$ versus $x_2^* < 0$ restricted to streamlines with $x_1^* \geq 0$, corresponding to abstract patches versus quasi-abstract patches, respectively. Each streamline is color-coded according to its AR ID. The color palette strip on the right indicates the mapping between AR IDs and their assigned colors.

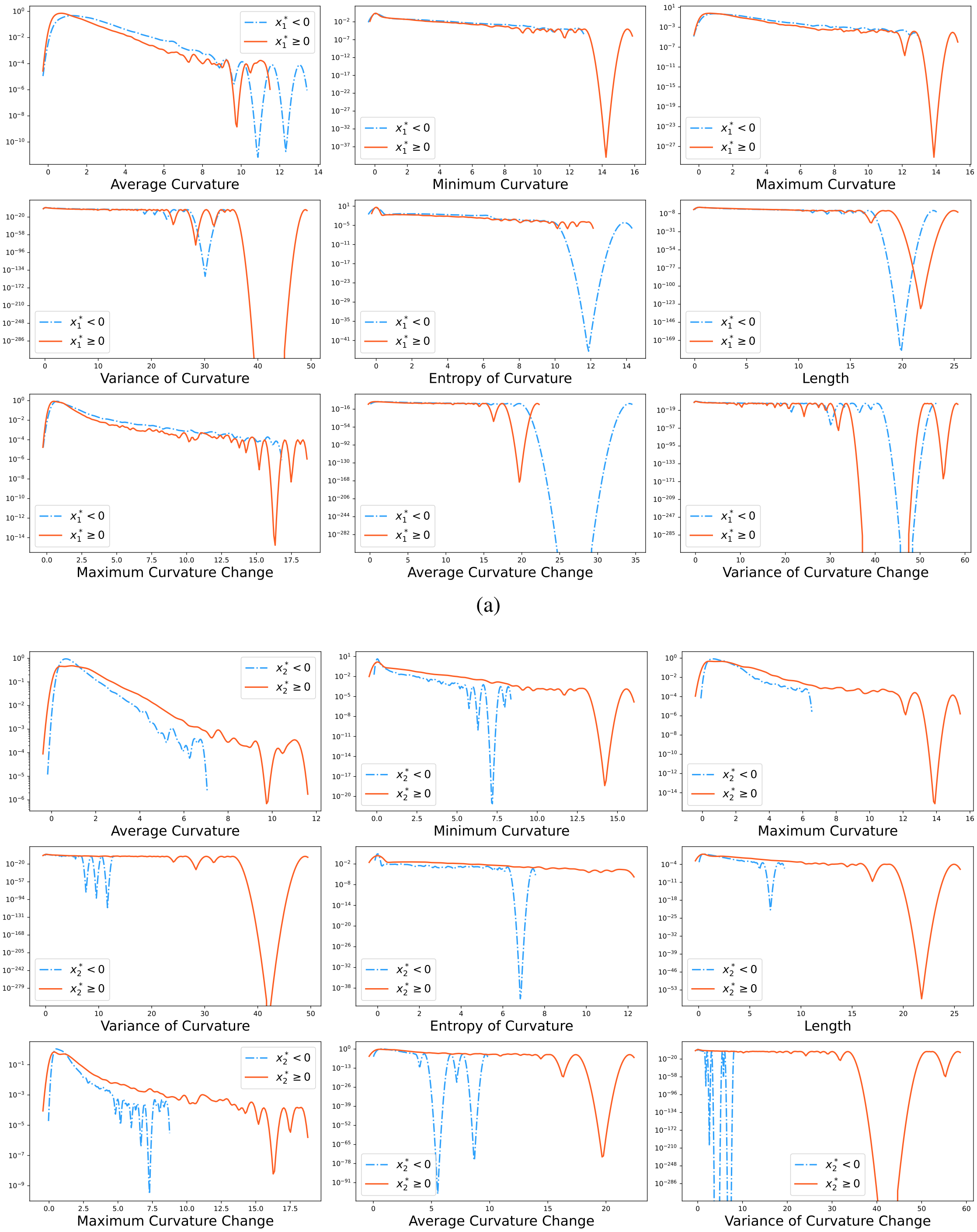

(a)

(b)

Fig. 6: Comparison of kernel density functions (KDFs) for each original geometric feature across different data subsets. (a) KDFs estimated for streamlines with $x_1^* < 0$ (strongly non-abstract) versus $x_1^* \geq 0$ (generalized abstract). (b) KDFs estimated for streamlines restricted to $x_1^* \geq 0$, further divided into two subsets: $x_2^* < 0$ (quasi-abstract) versus $x_2^* \geq 0$ (abstract).

ID	**Date**	**Title**	**Dimensions (cm)**	**Museum**
1	1906	Water Lilies	89.9 × 94.1	Art Institute of Chicago
2	1915–1926	Water Lilies (Agapanthus)	201.3 × 425.6	Cleveland Museum of Art
3	1897–1898	Nymphéas	66.04 × 104.14	Los Angeles County Museum of Art
4	1900	Water Lily Pond	89.8 × 101	Art Institute of Chicago
5	1917–1919	Water Lily Pond	130.2 × 201.9	Art Institute of Chicago
6	1904	Les Nymphéas	89.5 × 93.5	Musée d'Art Moderne
7	1907	Water Lilies (Nymphéas)	92.1 × 81.2	Museum of Fine Arts Houston
8	1907	Water Lilies	92.5 × 73.5	Kawamura Memorial DIC Museum of Art
9	1916–1919	Nymphéas Bleus	204.0 × 200.0	Musée d'Orsay
10	1899	The Water-Lily Pond	88.3 × 93.1	The National Gallery
11	1916	Water Lilies	200.5 × 201	National Museum of Western Art
12	1908	Water Lilies	Diameter: 80.01	Dallas Museum of Art
13	1914–1917	Water Lilies	166.05 × 142.24	Legion of Honor
14	1899	Japanese Footbridge and the Water Lily Pool, Giverny	89.2 × 93.3	Philadelphia Museum of Art
15	1922	Water Lilies	200.66 × 213.36	Toledo Museum of Art
16	1918	The Water-Lily Pond	131 × 197	Museum Barberini Potsdam
17	1915–1926	Water Lilies	200.7 × 426.1	Nelson-Atkins Museum of Art
18	1915–1926	Water Lilies (Nymphéas)	197.96 × 596.58	Carnegie Museum of Art
19	1917–1919	The Water-Lily Pond	100 × 200	Albertina Museum
20	1908	Water Lilies	101.0 × 90.0	Tokyo Fuji Art Museum
22	1914–1917	Nymphéas (Waterlilies)	181 × 201.6	National Gallery of Australia
23	1914–1917	Seerosen	200 × 200	Museum Barberini Potsdam
24	1916–1922	Le Bassin Aux Nymphéas, le soir	200 × 600	Kunsthaus Zürich
25	1920–1926	Le Bassin Aux Nymphéas, reflets verts	200 × 425	Kunsthaus Zürich
26	1920–1924	Japanese Bridge over the Water–Lily Pond in Giverny	90 × 92.5	Museu de Arte de São Paulo Assis Chateaubriand
27	1915–1926	Soleil Couchant	200 × 600	Musée de l'Orangerie
28	1915–1926	Reflets verts (Les Nymphéas)	200 × 850	Musée de l'Orangerie
29	1915–1926	Le Matin clair aux saules	200 × 1275	Musée de l'Orangerie
30	1916–1919	Nymphéas avec rameaux de saule	160 × 180	Musée des Impressionnismes Giverny
31	1915–1926	Water Lilies	200 × 426.1	Saint Louis Art Museum
32	1899	The Japanese Footbridge	81.3 × 101.6	National Gallery of Art
33	1906	Water Lilies	73.0 × 92.5	Ōhara Museum of Art Main Gallery
34	1918–1926	Nymphéas, Japanese Bridge	88.9 × 92.7	Philadelphia Museum of Art
35	1899	Water Lilies and Japanese Bridge	90.5 × 89.7	Princeton University Museum of Art
36	1903	The Water Lily Pond (Clouds)	4.61 × 107.95	Dallas Museum of Fine Arts
37	After 1916	Water Lilies	200.7 × 426.7	The National Gallery, London
38	1897–1898	Water Lilies	89.0 × 130.0	Kagoshima City Museum of Art
39	1905	Waterlilies	81.9 × 101.0	National Museum Wales
40	1908	Waterlilies	100.7 × 81.3	National Museum Wales
41	1906	Waterlilies	81.6 × 92.7	National Museum Wales
42	1907	Nymphéas	Diameter: 80.7	Musée d'Art Moderne et Contemporain de Saint-Étienne Métropole
43	c. 1907	Water Lilies, Setting Sun	73 × 92.7	National Gallery, London
44	1903	Water Lilies	—	Artizon Museum
45	1907	Water Lilies	—	Artizon Museum
46	1907	Water Lilies	100 × 81	Kuboso Memorial Museum of Art, Osaka
47	1904	Waterlilies or The Water Lily Pond (Nymphéas)	87.95 × 91.44	Denver Art Museum
48	1914–1915	Waterlilies	160.7 × 180.7	Portland Art Museum, Oregon
49	1916	Water Lilies, Reflections of Weeping Willows	199.3 × 424.4	National Museum of Western Art
50	1915–1917	Nymphéas Blancs et Jaunes	200 × 200	Kunstmuseum Winterthur
51	1916–1919	Water Lily, Willow Shadow	130.0 × 197.7	Municipal Museum of Art, Kitakyushu
52	1922	The Japanese Footbridge, Giverny	88.9 × 94.1	Museum of Fine Arts Houston
53	1923–1925	The Japanese Bridge	88.9 × 116.21	Minneapolis Institute of Art
54	Early 1920s	Waterlily Pond and Japanese Bridge in Monet's Garden in Giverny	—	Musée Marmottan Monet
55	1903	Waterlilies	73 × 92	Musée Marmottan Monet

TABLE 1: Catalogue of Claude Monet's *Water Lilies* used in our analysis, ordered by painting ID. The table includes each work's production date, title, physical dimensions, and current holding institution.

ID	Date	Title	Dimensions (cm)	Museum
56	1916–1919	Waterlilies with Reflections of a Willow Tree	131 × 155	Musée Marmottan Monet
57	1916–1919	Waterlilies with Reflections of a Willow Tree	200 × 200	Musée Marmottan Monet
58	1916–1919	Waterlilies	130 × 152	Musée Marmottan Monet
59	1916–1919	Waterlilies	200 × 180	Musée Marmottan Monet
60	1907	Water Lilies	100 × 73	Musée Marmottan Monet
61	1908	Waterlilies	—	Private Collection
62	1919	The Water Lily Pond	99.6 × 103.7	Private Collection
63	1919	Water Lilies	101 × 200	Metropolitan Museum of Art
64	1916–1919	Waterlilies	130.2 × 200.7	Metropolitan Museum of Art
65	1919	Le Bassin Aux Nympheas	100.4 × 201	Private Collection
66	1918	The Japanese Bridge	100 × 200	Musée Marmottan Monet
67	1914–1917	Water Lilies	200 × 200	Musée Marmottan Monet
68	1904	The Waterlily Pond	90 × 92	Private Collection
69	1915–1926	Les Nuages (The Water Lilies – The Clouds)	1275 × 200	Musée de l'Orangerie
70	1915–1926	Matin (The Water Lilies – Morning)	1275 × 200	Musée de l'Orangerie
71	1907	Pond with Water Lilies	101.5 × 72	The Israel Museum, Jerusalem
72	1915–1926	Les Deux Saules (The Water Lilies – The Two Willows)	1700 × 200	Musée de l'Orangerie
73	1915–1926	The Water Lilies – Morning with Willows	1275 × 200	Musée de l'Orangerie
74	1915–1926	Reflets d'Arbres (The Water Lilies – Tree Reflections)	850 × 200	Musée de l'Orangerie
75	Um 1916	Le Bassin Aux Nymphéas (The Water-Lily Pond)	131.2 × 201.3	Museum Folkwang, Essen, Germany
76	1914–1922	Le Bassin Aux Nymphéas Avec Iris (The Water Lily Pond with Irises)	200 × 600	Kunsthaus Zurich, Switzerland
77	1914–1917	Le bassin Aux Nymphéas (The Water-Lily Pond)	301 × 200.5	Fondation Beyeler, Riehen, Switzerland

TABLE 1: Catalogue of Claude Monet's *Water Lilies* used in our analysis, ordered by painting ID. The table includes each work's production date, title, physical dimensions, and current holding institution. Continued from previous page.

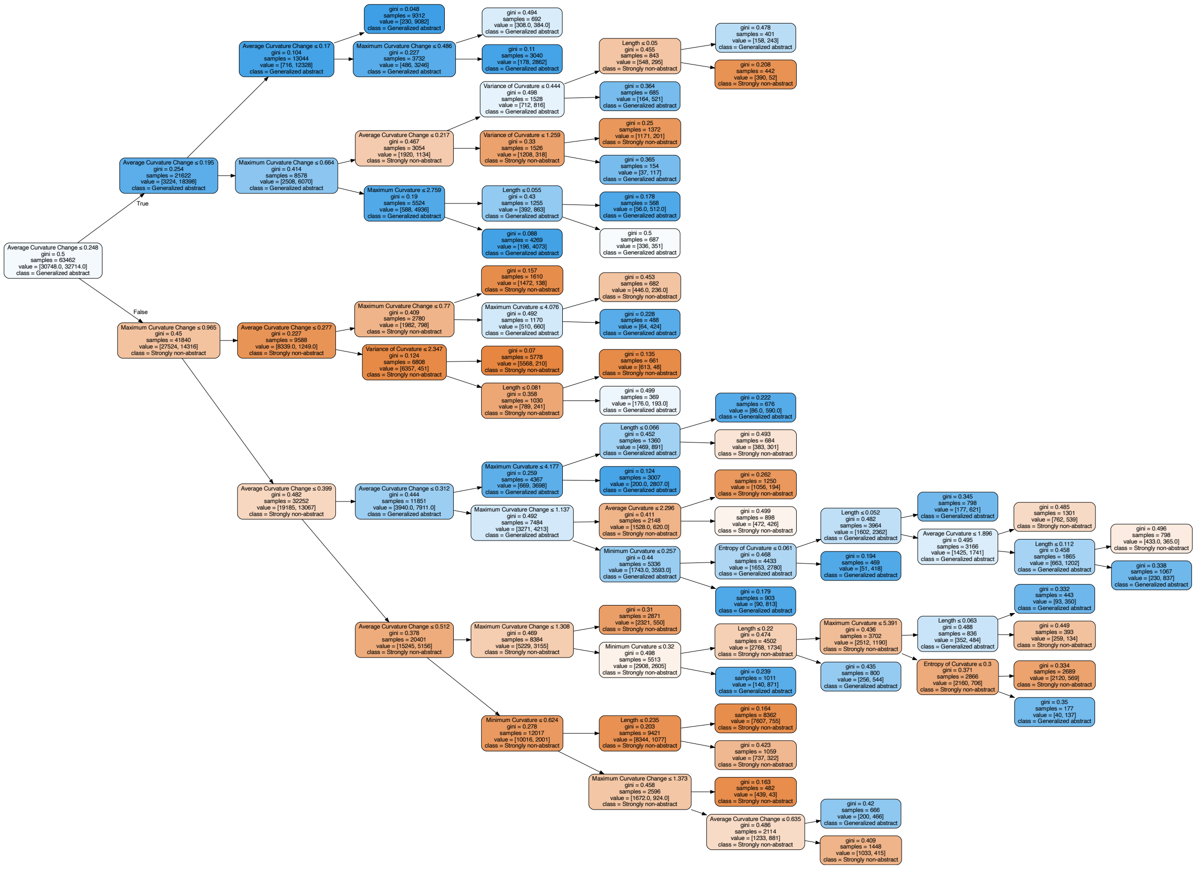

Fig. 7: Decision tree for classifying generalized abstract ($x_1^* \geq 0$) versus strongly non-abstract ($x_1^* < 0$) cases. The tree contains 40 leaf nodes. Nodes classified as generalized abstract are shaded in blue; those classified as strongly non-abstract are shaded in orange.

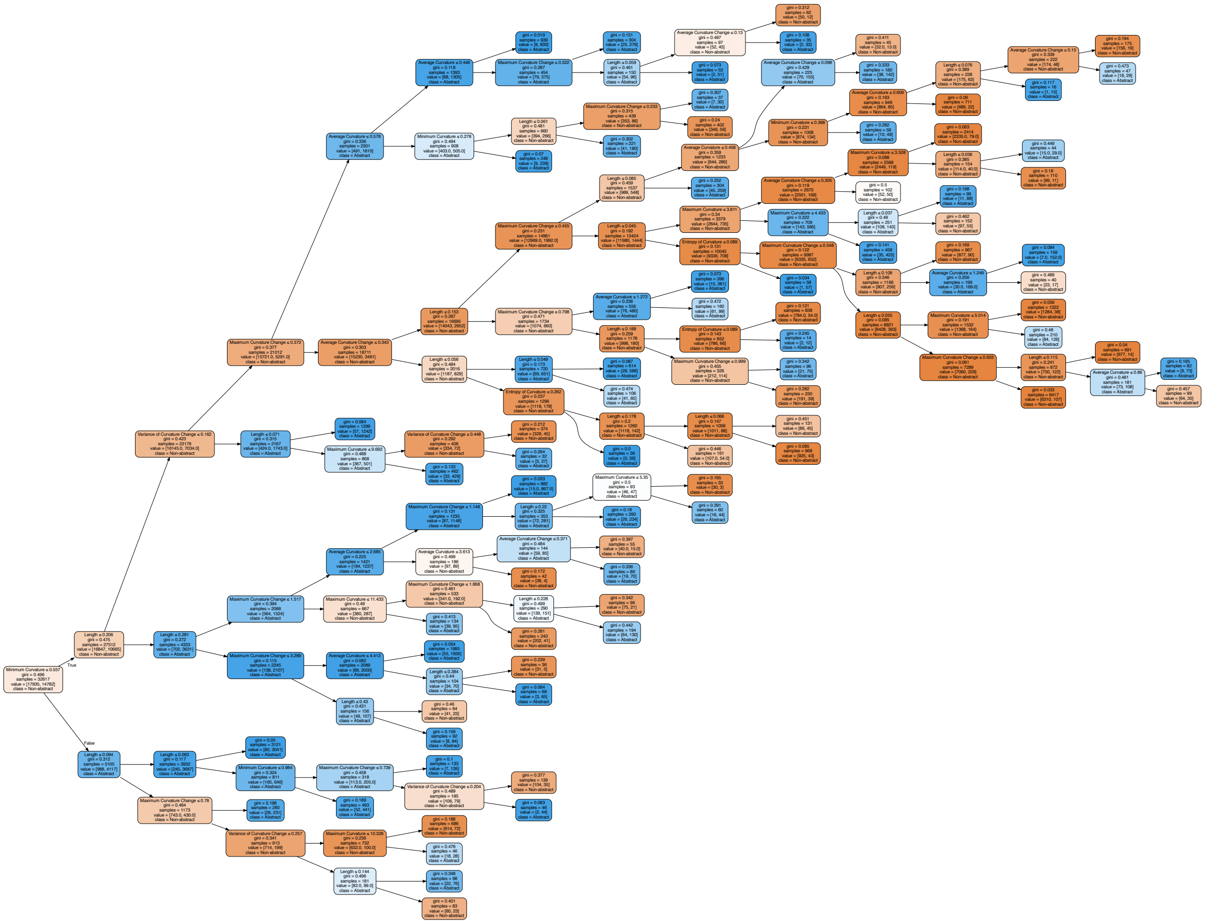

Fig. 8: Decision tree for classifying abstract ($x_2^* \geq 0$) versus quasi-abstract ($x_2^* < 0$) cases restricted to those in the generalized abstract class ($x_1^* \geq 0$). The tree contains 76 leaf nodes. Nodes classified as abstract are shaded in blue; those classified as quasi-abstract are shaded in orange.